Materials Research Bulletin 198 (2026) 114011

Contents lists available at ScienceDirect

Materials Research Bulletin

journal homepage: www.elsevier.com/locate/matresbu

Research Papers

Structural and luminescence analysis of Li^+/Na^+ co-doped $K_7CaGd_2(B_5O_{10})_3:Tb^{3+}$ phosphors with enhanced green emission and thermal stability

S. Yusan [a], M.B. Coban [b], U.H. Kaynar [c,d], I.G. Kaptanoglu [a], Abeer S. Altowyan [e,*], Jabir Hakami [f], H. Aydin [g,h], E.E. Karali [a], A. Canimoglu [i], N. Can [f,*]

[a] Ege University, Department of Nuclear Technology, Institute of Nuclear Sciences, Bornova, Izmir, Turkiye
[b] Balikesir University, Faculty of Arts and Sciences, Department of Physics, Balikesir, Turkiye
[c] Bakircay University, Faculty of Engineering and Architecture, Department of Fundamental Sciences, Menemen, Izmir, Turkiye
[d] Bakircay University, Biomedical Technologies Design Application and Research Center, Menemen, Izmir, Turkiye
[e] Department of Physics, College of Science, Princess Nourah Bint Abdulrahman University, P.O. Box 84428, Riyadh 11671, Saudi Arabia
[f] Jazan University, College of Science, Department of Physical Sciences, Physics Division, P.O. Box 114, 45142 Jazan, Kingdom of Saudi Arabia
[g] Central Research Laboratories, Izmir, Katip Celebi University, Turkiye
[h] Graphene Application&Research Center, Izmir, Katip Celebi University, Turkiye
[i] Omer Halisdemir University, Faculty of Arts and Sciences, Physics Department, Nigde, Turkiye

ARTICLE INFO

Keywords:
Microwave-assisted synthesis
Judd–Ofelt analysis
Tb^{3+}-activated phosphors
Green emission
Alkali co-doping
Borate materials

ABSTRACT

Li^+/Na^+ co-doped $K_7CaGd_2(B_5O_{10})_3:Tb^{3+}$ (KCGBO) green phosphors were synthesized via a microwave-assisted combustion method. XRD confirmed a pure rhombohedral phase (R32). Under 378 nm excitation, strong green emission at ~544 nm ($^5D_4 \rightarrow {}^7F_5$) was observed, optimized at 3 wt% Tb^{3+} before quenching. Li^+/Na^+ co-doping enhanced luminescence through local field distortion and improved energy transfer. Judd–Ofelt analysis revealed superior radiative efficiency for Li^+ co-doped samples ($A_J = 1.12 \times 10^6\ s^{-1}$, $\tau_{rad} = 0.089$ ms, $G = 1.08 \times 10^{-22}\ cm^2$). Thermal studies showed 82% intensity retention at 450 K with partial anti-thermal quenching and activation energy of ~0.52 eV, indicating suppressed non-radiative losses. The results demonstrate that Li^+/Na^+ co-doping and optimized Tb^{3+} content synergistically improve emission efficiency and thermal stability, making KCGBO:Tb^{3+} a promising green phosphor for near-UV solid-state lighting.

1. Introduction

The continuous pursuit of highly efficient and thermally stable phosphors for solid-state lighting has motivated extensive exploration of borate-based hosts due to their rich structural diversity, wide band gaps, and strong chemical and thermal stability [1–3]. The borate framework, composed of $[BO_3]$ and $[BO_4]$ units or complex $[B_5O_{10}]$ polyanions, provides a rigid covalent network with low phonon energy, favorable for suppressing non-radiative relaxation of excited rare-earth (RE^{3+}) ions. Such characteristics make borates ideal hosts for photoluminescent materials and nonlinear optical crystals [4].

The $K_7CaR_2(B_5O_{10})_3$ ($R = Y$, Nd, Yb, Gd) family of borates has recently gained considerable attention owing to its noncentrosymmetric trigonal R32 structure, broad UV transparency window, and excellent structural stability, as demonstrated in both experimental and theoretical studies [5,6]. Within this family, $K_7CaGd_2(B_5O_{10})_3$ represents a structurally analogous host to $K_7CaY_2(B_5O_{10})_3$ (KCYB), but has not yet been explored for Tb^{3+} activation. Previous research on KCYB:Eu^{3+} phosphors revealed intense red emission and high thermal stability, further enhanced through Sm^{3+} or Gd^{3+} co-doping via efficient energy transfer processes [7]. These findings suggest that the $[B_5O_{10}]$-based lattice provides favorable crystal fields and energy-migration pathways for rare-earth ions. However, the luminescent behavior of Tb^{3+}-activated $K_7CaGd_2(B_5O_{10})_3$ (KCGB) phosphors remains unexplored, offering new opportunities in the green-emission region of the visible spectrum.

The Tb^{3+} ion is a well-known green emitter, characterized by sharp $^5D_4 \rightarrow {}^7F_5$ transitions around 540 nm under UV or blue excitation. Its sharp line emission, high color purity, and relatively long lifetime make Tb^{3+} a promising activator for green components in phosphor-converted white LEDs and display technologies [8–11]. The luminescence efficiency of Tb^{3+}, however, is highly dependent on the host environment, particularly the crystal field symmetry, phonon energy, and defect

* Corresponding authors.
E-mail addresses: asaltowyan@pnu.edu.sa (A.S. Altowyan), ncan@jazanu.edu.sa (N. Can).

https://doi.org/10.1016/j.materresbull.2026.114011
Received 7 November 2025; Received in revised form 26 December 2025; Accepted 13 January 2026
Available online 14 January 2026

concentration. Therefore, lattice engineering strategies—such as alkali ion co-doping—are crucial to optimizing its performance.

In recent years, Li^+ and Na^+ co-doping has emerged as an effective approach to modulate structural and optical properties of RE^{3+}-activated phosphors. The introduction of small alkali ions can (i) compensate local charge imbalance, (ii) promote crystallinity and grain growth, (iii) alter the local symmetry around the luminescent center, and (iv) reduce non-radiative defects [10,12,13]. Enhanced emission intensities and improved thermal stability have been widely reported in borate hosts upon Li^+/Na^+ incorporation, such as in Eu^{3+}-, Sm^{3+}-, and Dy^{3+}-doped systems [14,15]. Therefore, applying Li^+/Na^+ co-doping to the Tb^{3+}-activated KCGB compound represents a rational strategy for improving photoluminescence efficiency and color purity.

Given the established structural robustness of KCYB and its demonstrated suitability for RE^{3+} substitution, the $K_7CaGd_2(B_5O_{10})_3$:Tb^{3+},Li^+/Na^+ system presents an unexplored yet promising platform for high-performance green-emitting phosphors. This work aims to synthesize and characterize this novel composition, investigating the effects of Li^+ and Na^+ co-doping on the structural, morphological, and optical properties. Comprehensive analyses including *X*-ray diffraction (phase purity and lattice parameters), Raman/FTIR (borate vibration modes), SEM–EDS (microstructure and dopant verification), and photoluminescence (excitation/emission spectra, decay dynamics, and Judd–Ofelt analysis) will be conducted to elucidate the role of alkali codopants in modulating luminescence behavior.

In particular, Judd–Ofelt (J–O) theory [16,17] will be applied to evaluate intensity parameters (Ω_2, Ω_4, Ω_6), radiative transition probabilities, and internal quantum efficiencies. The combined structural and spectroscopic insights are expected to clarify how Li^+/Na^+ co-doping influences the local environment and radiative processes of Tb^{3+} ions within the KCGBO host lattice. The results will contribute to the broader understanding of [B_5O_{10}]-borate-based as versatile matrices for rare-earth phosphors and pave the way for developing thermally robust, high-brightness green emitters suitable for n-UV excited solid-state lighting applications.

2. Experiments

2.1. Synthesis of $K_7CaGd_2(B_5O_{10})_3$:Tb^{3+},Li^+/Na^+ nanophosphors

Nanocrystalline samples of KCGBO were synthesized for the first time via a microwave-assisted combustion route combined with a sol–gel technique. High-purity analytical-grade precursors—Gadolinium (III) oxide (Gd_2O_3, Sigma-Aldrich, >99.9 %), potassium nitrate (KNO_3, ≥99.0 %), calcium nitrate ($Ca(NO_3)_2$, ≥99.5 %), and boric acid (H_3BO_3, ≥99.5 %)—were used as oxidizing agents, while urea (CH_4N_2O) and glycine ($C_2H_5NO_2$) served as organic fuels to initiate the exothermic combustion reaction. All chemicals were weighed in stoichiometric proportions according to the desired molar composition of KCGBO and thoroughly mixed in a beaker.

To investigate the activator effect, Terbium (III) nitrate hydrate ($Tb(NO_3)_3{\cdot}xH_2O$, 99.9 %, Sigma-Aldrich) was introduced as a rare-earth dopant at varying concentrations of 0.5, 1, 2, 3, 5, and 7 wt % relative to the host matrix. For the co-doping studies, sodium nitrate ($NaNO_3$, 99.9 %, Merck) and lithium nitrate ($LiNO_3$, 99.9 %, Merck) were incorporated into the precursor mixture at identical weight percentages to evaluate the influence of Na^+ and Li^+ ions on the structural and luminescent properties. In addition, a series of Li^+ and Na^+ co-doping levels (y = 0.005, 0.01, 0.02, 0.03, 0.05, and 0.07) was synthesized to identify the optimal alkali concentration for PL enhancement. Based on this optimization, the structural analysis (XRD) focused on the compositions with the highest emission intensity (0.03 Li^+ and 0.02 Na^+).In the first stage of synthesis, Gd_2O_3 was dissolved in 1 N nitric acid under gentle heating in a quartz beaker until a clear solution was obtained. The corresponding nitrate salts of K^+, Ca^{2+}, and Tb^{3+}, along with H_3BO_3, were then added to the solution. Subsequently, 20 mL of deionized water was introduced to ensure complete dissolution of all components. The calculated amounts of urea and glycine were added as fuels, and the solution was magnetically stirred at 80 °C for 1 h to obtain a homogeneous sol. The mixture was then partially uncovered and continuously stirred until the excess water evaporated and a viscous gel was formed. Gel formation occurred after approximately 45–60 min of heating at 80 °C, when the solution reached a thick, transparent, and uniformly viscous consistency, indicating complete polymerization of the sol.

The resulting gel was placed in a domestic microwave oven (2.45 GHz, 800 W) to trigger the combustion reaction. The self-ignition occurred within seconds, accompanied by the rapid evolution of gases and formation of white, porous, voluminous powders—indicative of complete combustion. The microwave irradiation was applied for a total of 6–8 min, during which the gel temperature rapidly increased to approximately 450–550 °C due to the exothermic combustion reaction. The as-burned powders were loosely agglomerated and were collected without further washing.

To achieve complete crystallization and remove any residual organic species, the obtained powders were annealed at 920 °C for 4 h in air using an alumina crucible. After cooling naturally to room temperature, fine white nanocrystalline KCGBO powders were obtained. All samples were stored in a desiccator prior to structural and optical characterization to prevent moisture absorption.

2.2. Characterization

X-ray diffraction (XRD) measurements were performed on a Malvern PANalytical Empyrean diffractometer employing Cu Kα radiation (λ = 1.5406 Å) operated at 45 kV and 40 mA. Diffraction data were collected in the 2θ range of 10°–80° with a step size of 0.02° and a scan rate of 1° min^{-1}. Structural refinement and phase identification were carried out using the Rietveld method implemented in *HighScore Plus* software. Fourier-transform infrared (FTIR) spectra were acquired on a *Thermo Scientific Nicolet iS50* spectrometer in the 4000–400 cm^{-1} range using the attenuated total reflectance (ATR) method. Each spectrum was averaged over 32 scans at a spectral resolution of 4 cm^{-1} to ensure accurate identification of the borate vibrational modes. Raman spectroscopy was conducted on a *Renishaw inVia Reflex* spectrometer equipped with a 532 nm excitation laser and a 2400 lines mm^{-1} grating. The laser power was kept below 1 mW to avoid local heating, and each spectrum was collected in the 200–1600 cm^{-1} range with an accumulation time of 10 s per scan. Surface morphology and chemical composition were analyzed using a *ZEISS GeminiSEM 500* scanning electron microscope (SEM) operated at 10 kV accelerating voltage, coupled with energy-dispersive *X*-ray spectroscopy (EDS) for elemental mapping. All samples were sputter-coated with a thin (~10 nm) gold layer to minimize surface charging during imaging. Photoluminescence (PL) excitation and emission spectra were recorded on an *Edinburgh Instruments FS5 spectrofluorometer* equipped with a 150 W xenon arc lamp as the excitation source. The slit width was maintained at 2.5 nm for both excitation and emission channels. Fluorescence decay profiles were measured using a pulsed xenon lamp with a 5 μs dwell time, and the average lifetimes were obtained from multi-exponential fitting. To assess thermal stability, temperature-dependent PL spectra were collected in the 300–550 K range using a *Linkam THMS600* variable-temperature stage. The samples were heated at a rate of 5 °C min^{-1} to the desired temperature, held for 5 min for thermal equilibrium, and then allowed to cool naturally to room temperature at approximately 3 °C min^{-1}. This procedure ensured reproducible evaluation of thermal quenching and trap-assisted luminescence behavior.

3. Results and discussions

3.1. X-ray diffraction and Rietveld refinement

Powder *X*-ray diffraction (PXRD) patterns recorded for the undoped

and doped $K_7CaGd_2(B_5O_{10})_3$ (KCGBO) samples (Fig. 1a) are indexed to a trigonal R32 lattice built from isolated [B_5O_{10}] polyborate units. All major Bragg reflections coincide with the reference pattern (JCPDS 04–024–1070), which corresponds to the standard pattern for $K_7CaR_2(B_5O_{10})_3$-type structures, and no extra peaks attributable to secondary phases are detected within the instrumental background, indicating single-phase formation across the compositions studied (undoped; 0.01, 0.03, 0.05 Tb^{3+}; 0.03 Tb^{3+}–0.03 Li^+; 0.03 Tb^{3+}–0.02 Na^+).

Rietveld refinements were performed in R32 using the structural model derived from our CIF (starting atomic positions fixed to the reported framework), with a Thompson–Cox–Hastings pseudo-Voigt peak shape, a Chebyshev polynomial background, and refinement of scale factor, zero shift, lattice parameters, and profile parameters. Isotropic displacement factors for cations were refined with chemically reasonable constraints. Representative fits are shown in Fig. 1b (observed, calculated, and difference profiles), and the refined metric parameters and agreement indices are summarized in Table 1. All refined crystallographic parameters, including atomic positions (x, y, z), site occupancies, and isotropic displacement factors (B_{iso}), derived from the Rietveld analysis, are provided in Table 2. The refined structural model obtained from Rietveld analysis was visualized using the atomic coordinates from the CIF file (ICSD No. 4126,820) to better illustrate the atomic arrangement within the KCGBO lattice. Fig. 1c displays the crystal structure of $K_7CaGd_2(B_5O_{10})_3$ viewed along the [001] direction. The structure is composed of isolated [B_5O_{10}] polyborate groups (green polyhedra) interconnected through Ca^{2+} (blue spheres) and Gd^{3+}/Tb^{3+} (violet/grey spheres) octahedral sites, while K^+ ions (orange spheres) occupy large interstitial cavities and channels running parallel to the c-axis. This three-dimensional framework of alternating borate units and cationic channels accounts for the observed structural stability and optical transparency. The availability of both divalent (Ca^{2+}) and trivalent (Gd^{3+}) coordination environments provides chemically compatible substitutional sites for Tb^{3+} activators and Li^+/Na^+ co-dopants, in full agreement with the experimental phase purity confirmed by XRD.

For the undoped host, the refined cell constants are $a = b = 13.32902$ Å, $c = 15.06382$ Å, $V = 2317.73$ Å^3 with $R_p = 0.0479$, $R_{wp} = 0.0737$, and

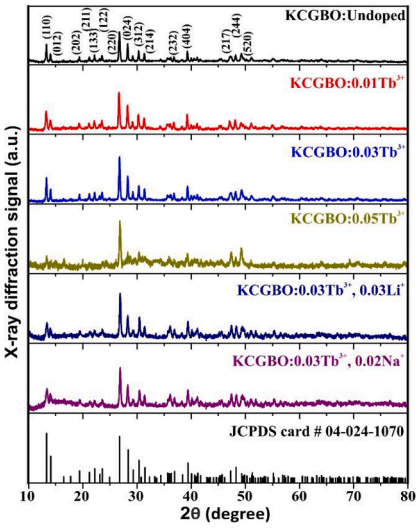

(a)

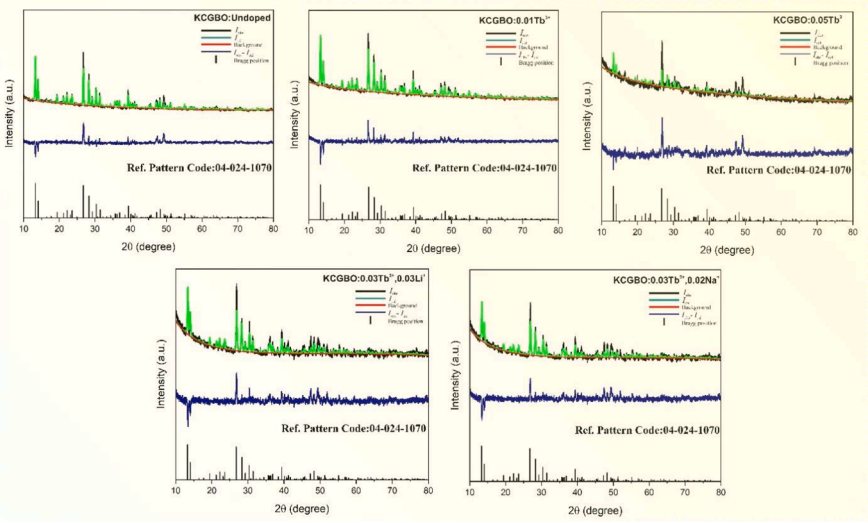

(b)

Fig. 1. (a) PXRD patterns of undoped and doped KCGBO samples, indexed to the trigonal R32 phase (JCPDS 04–024–1070). (b) Rietveld refinement profiles confirming phase purity and structural fitting. (c) Crystal structure of KCGBO viewed along the [001] direction, showing isolated [B_5O_{10}] units and cationic sublattices. (d) variation of average crystallite size estimated from Debye–Scherrer, Monshi–Scherrer, Williamson–Hall, Halder–Wagner, and Size–Strain models.

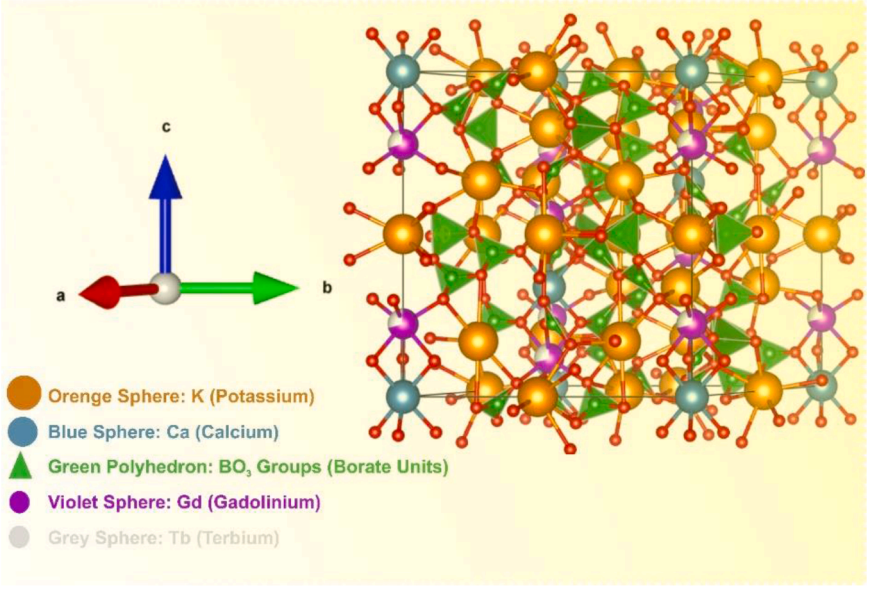

(c)

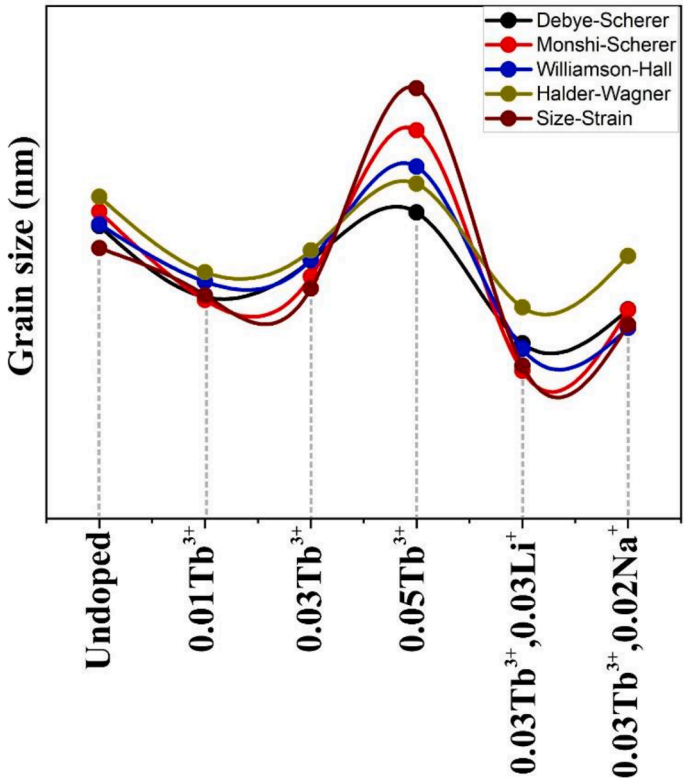

(d)

Fig. 1. (*continued*).

$\chi^2 = 2.623$, attesting to an excellent match between the structural model and experimental data. Upon Tb^{3+} substitution on the Gd^{3+} site (0.01–0.05 Tb^{3+}), a systematic contraction of the lattice is observed (e.g., at 0.05 Tb^{3+}: $a = b = 13.30683$ Å, $c = 15.0327$ Å, $V = 2305.24$ Å^3), which is consistent with the slightly smaller Shannon radius of Tb^{3+} relative to Gd^{3+} in octahedral coordination.

The feasibility of ionic substitution in the KCGBO lattice was evaluated using the ionic radius difference (D_r), following the commonly used solid-solution formation criterion described in solid-state chemistry literature [18]. The D_r parameter is defined as

Table 1
Refined lattice parameters and reliability factors obtained from Rietveld analysis of undoped and doped KCGBO samples. all samples crystallize in the trigonal R32 structure without secondary phases.

	KCGBO					
Unit Cell	Undoped	0.01Tb^{3+}	0.03Tb^{3+}	0.05Tb^{3+}	0.03Tb^{3+},0.03Li^{+}	0.03Tb^{3+},0.02Na^{+}
a [Å]	13.32902	13.63514	13.32418	13.30683	13.26730	13.26989
b [Å]	13.32902	13.63514	13.32418	13.30683	13.26730	13.26989
c [Å]	15.06382	15.06749	15.05948	15.0327	15.13007	15.13481
α,β,γ [°]	90,90,120	90,90,120	90,90,120	90,90,120	90,90,120	90,90,120
Vol. [$Å^3$]	2317.727	2327.735	2315.376	2305.244	2306.410	2308.036
χ^2	2.6230	2.2632	2.6554	2.2550	2.0098	1.9410
R_p	0.0479	0.0466	0.0474	0.0539	0.0489	0.0481
R_{wp}	0.0737	0.0693	0.0727	0.0735	0.0687	0.0664
R_{exp}	0.0281	0.0306	0.0273	0.0326	0.0342	0.0342

$$D_r = \frac{|R_m(CN) - R_d(CN)|}{R_m(CN)} \times 100\% \quad (1)$$

where R_m and R_d denote the ionic radii (in Å) of the host cation and dopant, respectively, at the same coordination number (CN). Generally, a D_r value below 30 % suggests feasible substitution without substantial lattice distortion [18]. The ionic radii used in these calculations were obtained from Shannon's revised effective ionic radii tables [19]. As summarized in Table 3, the calculated D_r values for Tb^{3+}→Gd^{3+} (1.599 %), Tb^{3+}→Ca^{2+} (7.700 %), and Tb^{3+}→K^{+} (32.627 %) demonstrate that Tb^{3+} substitution at the Gd^{3+} site is highly favorable, while alkali co-doping (Li^{+}, Na^{+}) at the K^{+} site remains within acceptable limits for partial replacement. These results corroborate the XRD observations, confirming that Tb^{3+} incorporation does not induce any major lattice distortion, consistent with the retained R32 symmetry.

Co-doping with Li^{+} (nominally occupying the A-site in place of K^{+} as a charge compensator) yields a further marginal volume reduction (V = 2306.41 $Å^3$ for 0.03 Tb^{3+}–0.03 Li^{+}), whereas Na^{+} co-doping gives a comparable but slightly larger cell (V = 2308.04 $Å^3$ for 0.03 Tb^{3+}–0.02 Na^{+}), consistent with the ionic size sequence $Li^{+} < Na^{+} < K^{+}$. In all cases, the goodness-of-fit indices remain robust ($R_p \approx 0.046$–0.054, $R_{wp} \approx 0.066$–0.074, $\chi^2 \approx 1.94$–2.66), and the difference curves do not show any systematic misfit around the strongest reflections, confirming phase purity and successful incorporation of dopants without symmetry lowering.

The small 2θ shifts observed across compositions (most evident at the high-intensity reflections) track the refined cell volumes and reflect Vegard-like behavior of the solid solution. Because the [B_5O_{10}] framework is rigid, these changes arise primarily from cation-site substitutions (Tb^{3+}↔Gd^{3+} on the octahedral RE site; Li^{+}/Na^{+}↔K^{+} on the alkali site) and associated local charge-compensation/relaxation, in line with prior observations in $K_7CaR_2(B_5O_{10})_3$ analogues and other RE-borates [4,5]. The preservation of R32 symmetry throughout indicates that the KCGB lattice tolerates Tb^{3+} activation and alkali co-doping without forming parasitic phases—an advantageous prerequisite for reliable photoluminescence analysis. These results confirm that the crystal structure remains intact upon doping, validating the reliability of subsequent spectroscopic analyses.

To further evaluate the microstructural evolution induced by Tb^{3+} doping and Li^{+}/Na^{+} co-doping, the crystallite size (D) and lattice strain (ε) were estimated from the diffraction peak broadening using multiple approaches, including the Debye–Scherrer, Monshi–Scherrer, Williamson–Hall (W–H), Halder–Wagner (H–W), and Size–Strain Plot (SSP) methods, as outlined in Nath et al. [20]. The calculated results are summarized in Table 4 and visualized in Fig. 1d

The average crystallite size of undoped KCGBO was found to be approximately 75–80 nm, depending on the chosen model, confirming the nanocrystalline nature of the powders. Upon Tb^{3+} incorporation, the mean size exhibited a moderate variation: it slightly decreased for low doping levels (0.01 Tb^{3+} → ≈70 nm) due to defect-induced lattice distortion, and increased again at 0.05 Tb^{3+} (≈ 80–87 nm), suggesting partial coalescence of grains at higher Tb^{3+} concentrations.

The microstrain (ε), derived from the W–H and H–W analyses, remained below 1.5 × 10^{-2}, indicating minor lattice distortion and confirming that the KCGBO framework efficiently accommodates the dopant ions without severe stress accumulation. For Li^{+} and Na^{+} co-doped samples, the crystallite size slightly decreased (≈ 65–70 nm), consistent with the smaller ionic radius of Li^{+} and Na^{+}, which can locally disturb grain growth during combustion synthesis.

These results are consistent with the Rietveld refinements, confirming that the incorporation of Tb^{3+} and alkali ions modifies the lattice only subtly, maintaining high structural integrity and phase purity.

The consistent structural integrity confirmed by these analyses provides a reliable foundation for interpreting the photoluminescence properties discussed in the following section.

3.2. *Vibrational analysis (FTIR and Raman spectroscopy)*

The vibrational properties of the undoped and doped KCGBO samples were examined by Fourier-transform infrared (FTIR) and Raman spectroscopy to gain insight into the local bonding environment and lattice dynamics. Both spectra exhibit the characteristic fingerprints of the [B_5O_{10}] structural units, confirming that the borate framework remains intact upon Tb^{3+} incorporation and Li^{+}/Na^{+} co-doping.

In the FTIR spectra (Fig. 2a), all samples display well-defined absorption bands in the range 400–1600 cm^{-1}, corresponding to internal vibrations of borate groups. The broad feature around 1425 cm^{-1} arises from the stretching vibrations of trigonal [BO_3] units, while the bands at 1354, 1243, and 1196 cm^{-1} originate from asymmetric B–O stretching in distorted [BO_3] configurations [21]. The intense absorptions observed near 1027 and 931 cm^{-1} are assigned to stretching modes of tetrahedral [BO_4] units, confirming the coexistence of three- and four-coordinated boron. Low-frequency modes at 783, 731, 614, 559, and 494 cm^{-1} correspond to B–O–B bending and in-plane deformation vibrations within the [B_5O_{10}] linkage network [22,23]. These assignments are consistent with previously reported spectra for borate phosphors such as $K_7CaR_2(B_5O_{10})_3$ and related mixed borate hosts [1,2,5].

The Raman spectra (Fig. 2b) further substantiate these observations, exhibiting prominent bands between 400 and 1300 cm^{-1} that correspond to symmetric stretching and bending vibrations of borate units. The high-frequency region (above 1000 cm^{-1}) is dominated by ν_1 and ν_3 stretching modes of [BO_4] tetrahedra, whereas the intermediate region (700–950 cm^{-1}) originates from B–O–B linkages and [BO_3] asymmetric stretching. The weak, low-wavenumber features below 600 cm^{-1} are attributed to external lattice vibrations involving cation motion (K^{+}, Ca^{2+}, and Gd^{3+}) coupled to the borate network.

Notably, the spectra of Tb^{3+}-doped and co-doped KCGBO samples exhibit only minimal shifts in band position and no emergence of new modes, implying that dopant incorporation causes negligible distortion to the borate backbone. Slight variations in intensity can be associated with localized strain and changes in bond polarizability due to the substitution of Gd^{3+} by Tb^{3+} or the partial replacement of K^{+} by Li^{+}/Na^{+}.

Table 2
Refined atomic coordinates (*x, y, z*), site occupancies, and isotropic displacement parameters (B_{iso}/U_{iso}) for undoped and Li^+/Na^+ co-doped $K_7CaGd_2(B_5O_{10})_3$:Tb^{3+} samples obtained from Rietveld refinement.

Sample	Element	Occupancy	Name	x	y	z	B_{iso}/U_{iso}
Undoped	Ca	1	Ca1	0	0	0.5	0.63165
	Gd	1	Gd1	0	0	0.2758	0.78246
	K	1	K1	0.5095	0	0	3.34777
	K	1	K2	0.5343	0	0	2.06867
	K	1	K3	0	0	0	1.92655
	O	1	O1	0.1071	0.1658	0.2007	1.53176
	O	1	O2	0.1852	0.3442	0.1274	3.61622
	O	1	O3	0.1422	0.0801	0.1034	2.51083
	O	1	O4	0.3655	0.1034	0.0064	1.87917
	O	1	O5	0.0053	0.1875	0.0793	1.45281
	B	1	B1	0.0968	0.2286	0.1361	1.36595
	B	1	B2	0.1895	0.4144	0.0570	2.13183
	B	1	B3	0.2497	0	0	1.44491
0.01Tb^{3+}	Ca	1	Ca1	0	0	0.5	0.63165
	Gd	1	Gd1	0	0	0.27588	0.78246
	K	1	K1	0.5095	0	0	3.34777
	K	1	K2	0.5343	0	0.5	2.51083
	K	1	K3	0	0	0	1.92655
	O	1	O1	0.1071	0.1658	0.20073	1.53176
	O	1	O2	0.1852	0.34423	0.12743	3.61622
	O	1	O3	0.1422	0.08017	0.38747	2.51083
	O	1	O4	0.3655	0.10347	0.00647	1.87917
	O	1	O5	0.0053	0.18753	0.07933	1.45281
	B	1	B1	0.0968	0.22863	0.13613	1.36595
	B	1	B2	0.1895	0.41443	0.05703	2.13183
	B	1	B3	0.2497	0	0	1.44491
0.03Tb^{3+}	Ca	1	Ca1	0	0	0.5	0.63165
	Gd	1	Gd1	0	0	0.27588	0.78246
	K	1	K1	0.5095	0	0	3.34777
	K	1	K2	0.53436	0	0.5	2.06867
	K	1	K3	0	0	0	1.92655
	O	1	O1	0.10717	0.16583	0.20073	1.53176
	O	1	O2	0.18527	0.34423	0.12743	3.61622
	O	1	O3	0.14223	0.08017	0.38747	2.51083
	O	1	O4	0.36553	0.10347	0.00647	1.87917
	O	1	O5	0.00537	0.18753	0.07933	1.45281
	B	1	B1	0.09687	0.22863	0.13613	1.36595
	B	1	B2	0.18957	0.41443	0.05703	2.13183
	B	1	B3	0.24977	0	0	1.44491
	Ca	1	Ca1	0	0	0.5	0.63165
0.05Tb^{3+}	Gd	1	Gd1	0	0	0.27588	0.78246
	K	1	K1	0.5095	0	0	3.34777
	K	1	K2	0.5343	0	0.5	2.06867
	K	1	K3	0	0	0	1.92655
	O	1	O1	0.1071	0.16583	0.20073	1.53176
	O	1	O2	0.1852	0.34423	0.12743	3.61622
	O	1	O3	0.1422	0.08017	0.38747	2.51083
	O	1	O4	0.3655	0.10347	0.00647	1.87917
	O	1	O5	0.0053	0.18753	0.07933	1.45281
	B	1	B1	0.0968	0.22863	0.13613	1.36595
	B	1	B2	0.1895	0.41443	0.05703	2.13183
	B	1	B3	0.2497	0	0	1.44491
	Ca	1	Ca1	0	0	0.5	0.63165
0.03Tb^{3+},0.03Li^+	Gd	1	Gd1	0	0	0.27588	0.78246
	K	1	K1	0.5095	0	0	3.34777
	K	1	K2	0.53436	0	0.5	2.06567
	K	1	K3	0	0	0	1.92655
	O	1	O1	0.10717	0.16583	0.20073	1.53176
	O	1	O2	0.18527	0.34423	0.12743	3.61622
	O	1	O3	0.14223	0.08017	0.38747	2.51083
	O	1	O4	0.36553	0.10347	0.00647	1.87917
	O	1	O5	0.00537	0.18753	0.07933	1.45281
	B	1	B1	0.09687	0.22863	0.13613	1.36595
	B	1	B2	0.18957	0.41443	0.05703	2.13183
	B	1	B3	0.24977	0	0	1.44491
	Ca	1	Ca1	0	0	0.5	0.63165
0.03Tb^{3+},0.02Na^+	Gd	1	Gd1	0	0	0.27588	0.78246
	K	1	K1	0.5095	0	0	3.34777
	K	1	K2	0.5343	0	0.5	2.06867
	K	1	K3	0	0	0	1.92655
	O	1	O1	0.1071	0.16583	0.20073	1.53176
	O	1	O2	0.1852	0.34423	0.12743	3.61622
	O	1	O3	0.1422	0.08017	0.38747	2.51083

(*continued on next page*)

Table 2 (*continued*)

Sample	Element	Occupancy	Name	x	y	z	B_{iso}/U_{iso}
	O	1	O4	0.3655	0.10347	0.00647	1.87917
	O	1	O5	0.0053	0.18753	0.07933	1.45281
	B	1	B1	0.0968	0.22863	0.13613	1.36595
	B	1	B2	0.1895	0.41443	0.05703	2.13183
	B	1	B3	0.2497	0	0	1.44491

Table 3
Calculated ionic radius mismatch percentages (D_r) between host cations (K^+, Ca^{2+}, Gd^{3+}) and dopant Tb^{3+} ions based on Shannon radii for $CN = 6$. a mismatch below 30 % indicates favorable substitution and effective dopant incorporation.

	K		Tb			Ca		Tb			Gd		Tb	
D_r	R_m	*CN*	R_d	*CN*	D_r	R_m	*CN*	R_d	*CN*	D_r	R_m	*CN*	R_d	*CN*
32.62	1.38	6	0.92	6	**7.70**	1.00	6	0.923	6	**1.59**	0.93	6	0.92	6

Table 4
Crystallite size (D) and microstrain (ε or δ) values of undoped and doped KCGBO samples estimated using Debye–Scherrer, Monshi–Scherrer, Williamson–Hall, Halder–Wagner, and size–strain models.

Concentration		Undoped	$0.01Tb^{3+}$	$0.03Tb^{3+}$	$0.05Tb^{3+}$	$0.03Tb^{3+}$,$0.03Li^+$	$0.03Tb^{3+}$,$0.02Na^+$
Debye-Scherer	D (nm)	77.65	70.47	74.17	79.04	65.77	69.21
	$\delta \times 10^{-3}$ (nm^{-2})	0.16	0.20	0.18	0.16	0.23	0.20
Monshi-Scherrer	D (nm)	79.14	70.16	72.54	87.37	62.99	69.16
	$\delta \times 10^{-3}$ (nm^{-2})	0.15	0.20	0.19	0.13	0.25	0.20
Williamson-Hall	D (nm)	77.85	72.04	74.26	83.70	65.23	67.35
	$\varepsilon \times 10^{-3}$	3.12	2.37	1.71	1.64	1.92	1.27
Halder-Wagner	D (nm)	80.64	72.99	75.18	81.96	69.44	74.62
	$\varepsilon \times 10^{-3}$	8.50	9.91	8.37	12.52	15.93	9.95
Size-Strain	D (nm)	75.42	70.64	71.33	91.65	63.51	67.67
	$\varepsilon \times 10^{-3}$	1.91	1.65	1.69	3.40	4.24	1.69

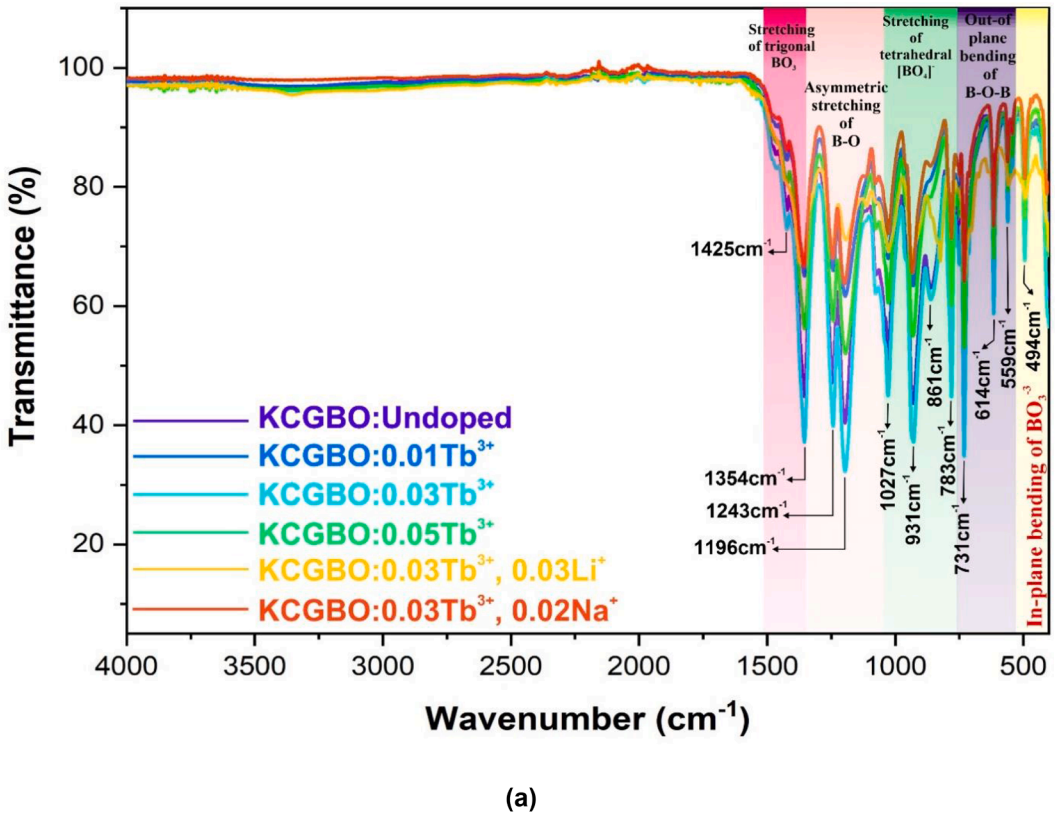

(a)

Fig. 2. (a) FTIR transmittance spectra of undoped and Tb^{3+}/Li^+/Na^+-doped $K_7CaGd_2(B_5O_{10})_3$ phosphors exhibiting characteristic vibrations of trigonal [BO_3] and tetrahedral [BO_4] units. (b) Raman spectra confirming the coexistence of [BO_3]/[BO_4] groups and the structural stability of the borate network upon doping.

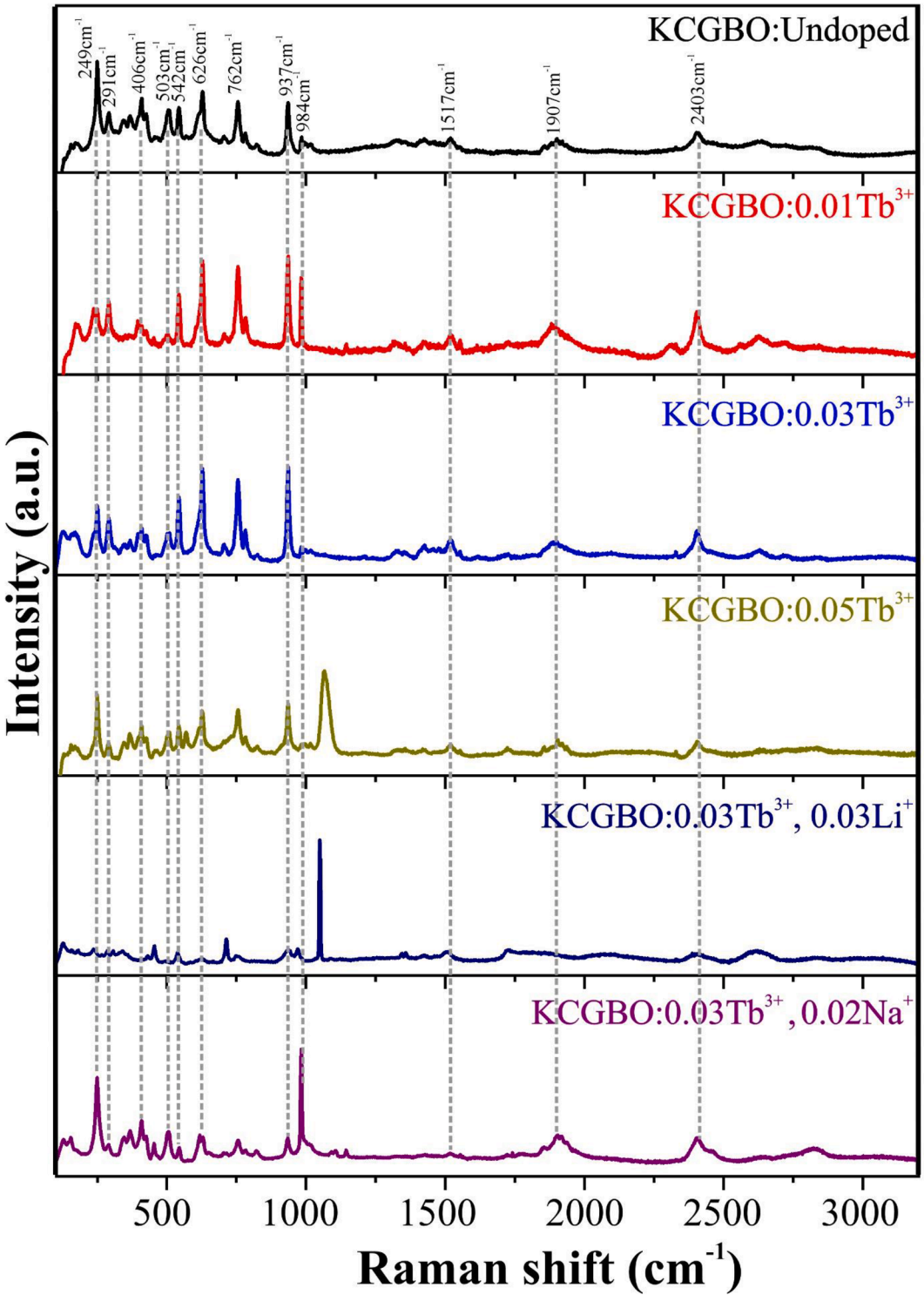

(b)

Fig. 2. (*continued*).

Together, the FTIR and Raman analyses confirm that the [B_5O_{10}] polyanionic framework is structurally robust and retains its integrity across all compositions. The combined vibrational evidence supports the XRD and Rietveld findings, demonstrating that Tb^{3+} activation and alkali co-doping occur without disrupting the crystalline symmetry—an essential prerequisite for efficient photoluminescence performance.

4. Photoluminescence studies

4.1. Photoluminescence excitation and emission characteristics of Tb^{3+} ions

The photoluminescence (PL) excitation and emission spectra of the $K_7CaGd_2(B_5O_{10})_3$: $0.005Tb^{3+}$ phosphor are presented in Fig. 3a. The

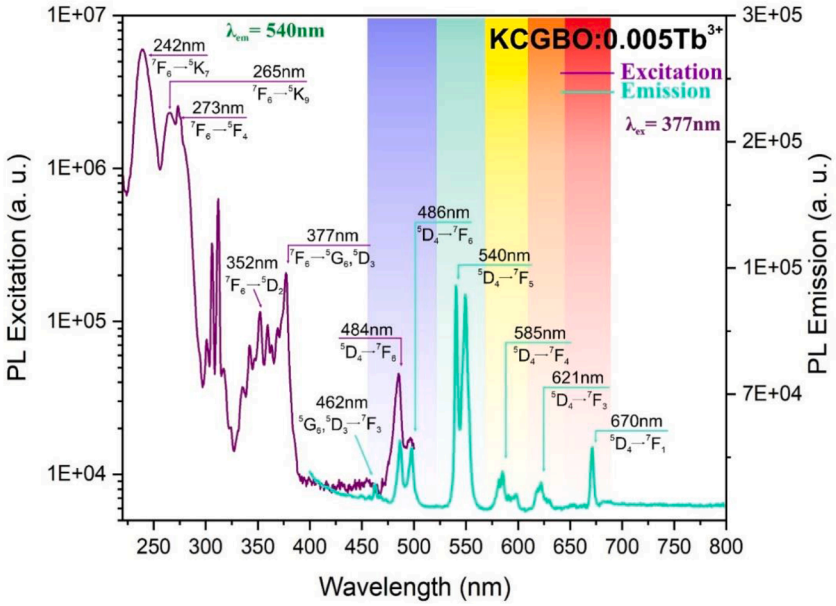

(a)

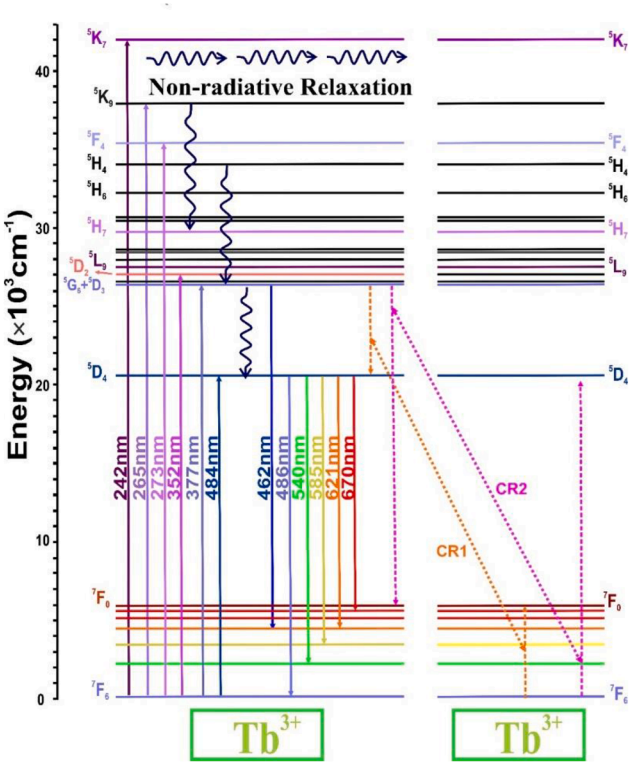

(b)

Fig. 3. (a) Photoluminescence excitation and emission spectra of $K_7CaGd_2(B_5O_{10})_3$: 0.005Tb^{3+} phosphor. (b) schematic energy level diagram of Tb^{3+} ions showing the excitation pathways, non-radiative relaxations, and radiative $^5D_4 \rightarrow {}^7F_j$ (J = 6–3) emissions. (c) PL emission spectra of $K_7CaGd_2(B_5O_{10})_3$: $x$$Tb^{3+}$ (x = 0.005–0.07) phosphors under 377 nm excitation, showing intensity variation and concentration quenching behavior with increasing Tb^{3+} content. (d) linear fitting of log(I/x) versus log(x) for KCGBO:$x$$Tb^{3+}$ phosphors used to determine the interaction parameter (Q).

excitation spectrum, monitored at an emission wavelength of 540 nm, reveals multiple sharp f–f transitions characteristic of Tb^{3+} ions, superimposed on a broad host-related band. The most intense excitation peak appears at 377 nm, which corresponds to the $^7F_6 \rightarrow {}^5G_6, {}^5D_3$ transitions of Tb^{3+}, making it the most efficient excitation channel for green emission under near-UV excitation [9,24,25]. Other notable excitation features are observed at 242 nm ($^7F_6 \rightarrow {}^5K_7$), 265 nm ($^7F_6 \rightarrow {}^5K_9$), 273 nm ($^7F_6 \rightarrow {}^5F_4$), and 352 nm ($^7F_6 \rightarrow {}^5D_2$), which are associated with higher $4f^8$–$4f^7 5d^1$

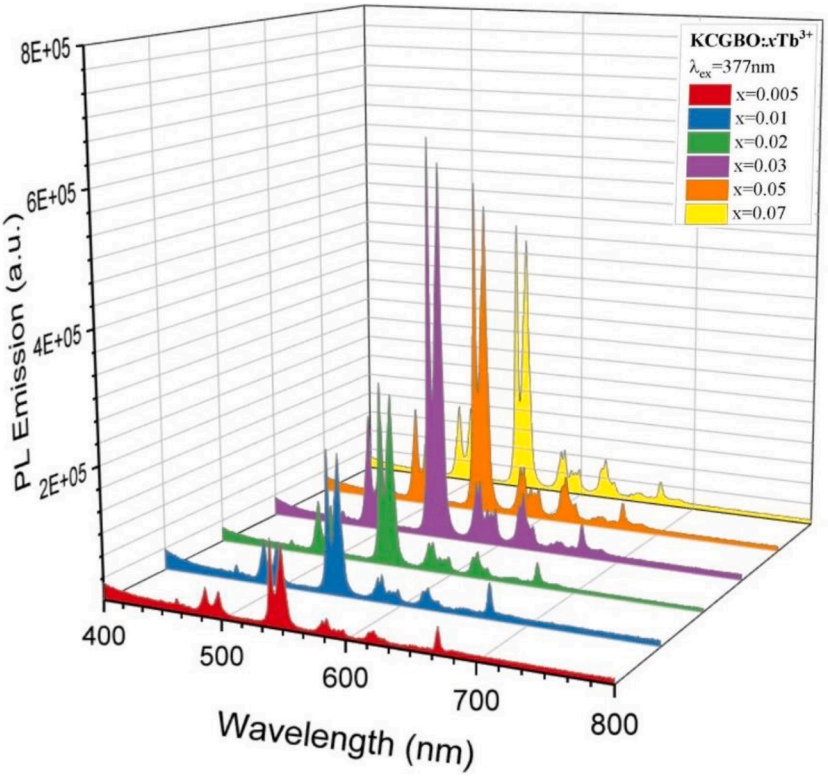

(c)

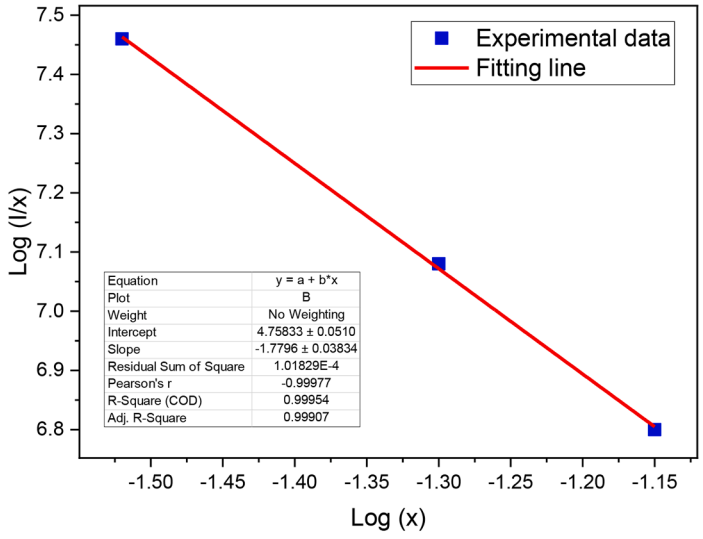

(d)

Fig. 3. (*continued*).

or interconfigurational transitions within the Tb^{3+} ion [26]. Although the bands at 242 and 265 nm show stronger apparent intensities due to host-related or 4f→5d absorptions, excitation in this deep-UV range is less practical for photoluminescent applications owing to higher nonradiative losses and instrumental limitations [26]. Therefore, the 377 nm excitation was selected for detailed emission analysis.

Upon excitation at 377 nm, the emission spectrum exhibits the well-known line pattern of Tb^{3+} arising from the $^5D_4 \rightarrow {}^7F_j$ (J = 6–3)

transitions. The corresponding energy level diagram of Tb^{3+} (Fig. 3b) illustrates the possible excitation and relaxation processes, confirming the assignment of the observed spectral transitions. The dominant emission band at 540 nm ($^5D_4 \rightarrow {}^7F_5$) corresponds to the characteristic green luminescence of Tb^{3+}, while weaker transitions at 486 nm ($^5D_4 \rightarrow {}^7F_6$), 585 nm ($^5D_4 \rightarrow {}^7F_4$), 621 nm ($^5D_4 \rightarrow {}^7F_3$), and 670 nm ($^5D_4 \rightarrow {}^7F_1$) account for blue, yellow, orange, and red components, respectively [27,28]. The predominance of the green emission peak indicates an efficient $^5D_4 \rightarrow {}^7F_5$ transition, consistent with electric-dipole-allowed $\Delta J = 1$ selection rules [29,30].

The energy-level configuration of Tb^{3+} ($4f^8$) favors a rapid nonradiative relaxation from the $^5D_3$ to $^5D_4$ levels, resulting in the suppression of blue emission and enhancement of the green line at 540 nm. This effect is further stabilized by the rigid borate lattice, which minimizes multiphonon relaxation owing to its wide band gap and low phonon energy (~1300 cm^{-1}) [7,31]. The excellent overlap between the near-UV excitation (377 nm) and visible green emission makes KCGBO:Tb^{3+} a promising candidate for green-emitting phosphors in near-UV-excited solid-state lighting systems.

To investigate the concentration dependence of luminescence, PL spectra were recorded for KCGBO:$x$$Tb^{3+}$ ($x = 0.005$–0.07) under 377 nm excitation, as shown in Fig. 3c. The emission intensity increases gradually up to $x = 0.03$, after which it decreases with further Tb^{3+} addition due to concentration quenching [32,33]. The critical distance (R_c) for energy migration can be estimated using the relation following Blasse's model [34], confirming that multipolar interactions dominate the quenching process in this system.

$$R_c = 2\left[\frac{3V}{4\pi x_c N}\right]^{1/3} \tag{2}$$

where V is the unit cell volume of the host lattice (2317.73 $Å^3$), x_c is the concentration of Tb^{3+} at the point of maximum emission intensity (0.03), and Z is the number of formula units per unit cell (3 for $K_7CaGd_2(B_5O_{10})_3$). Using these parameters, the average critical distance among Tb^{3+} ions in the KCGBO lattice was calculated to be approximately 37 Å, which is significantly larger than 5 Å. This suggests that, similar to the Tb^{3+}→Cr^{3+} system reported by Bai et al. [35], the concentration quenching in KCGBO:Tb^{3+} is primarily governed by electric multipolar interactions rather than exchange processes. In terms of multipolar coupling, several interaction types may occur, including dipole–dipole, dipole–quadrupole, and quadrupole–quadrupole interactions [36], among which the dipole–dipole type is predominant in the present host, as indicated by the large R_c value. The large R_c value further confirms that dipole–dipole coupling dominates the self-quenching behavior of Tb^{3+} ions in this host lattice. Beyond simple multipolar coupling, concentration quenching in KCGBO:Tb^{3+} is strongly influenced by energy migration through the lattice, where excitation hops among Tb^{3+} ions until it encounters defect-rich or distorted regions that act as quenching sinks. The borate network, with its low phonon energy, minimizes multiphonon relaxation, making migration-assisted trapping the dominant nonradiative pathway. As the Tb^{3+} concentration increases, the average hopping distance decreases, increasing the probability that an exciton reaches a vacancy or defect site. This migration-assisted mechanism explains the abrupt decrease in emission intensity beyond $x = 0.03$ and provides a more physically meaningful interpretation than dipole–dipole coupling alone. This indicates that the concentration quenching process is governed not by exchange interactions but by electric multipolar interactions, particularly dipole–dipole coupling.

The nature of energy transfer among Tb^{3+} ions was further analyzed using Dexter's theory. According to this model, the relationship between emission intensity (I) and activator concentration (x) can be expressed as [37]:

$$\frac{I}{x} = k\left(1 + \beta x^{Q/3}\right)^{-1} \tag{3}$$

where k and β are host-dependent constants and Q represents the type of multipolar interaction. For $x \geq x_c$, this can be linearized as [26]:

$$log(I/x) = C - (Q/3)log\ x, \tag{4}$$

The slope of the fitted line ($-Q/3$) obtained from the $\log(I/x)$–$\log(x)$ plot was –1.77, giving $Q = 5.31$, which is close to the theoretical value of 6, suggesting that dipole–dipole interactions dominate the concentration quenching process in the KCGBO:Tb^{3+} system (Fig. 3d). Such a mechanism is typical for Tb^{3+}-activated borate lattices, where the large critical distance ($R_c > 5$ Å) facilitates multipolar coupling rather than exchange interactions.

4.2. Effect of Li^+ and Na^+ co-doping on the photoluminescence properties

To further enhance the optical performance and investigate charge compensation effects, Li^+ and Na^+ ions were co-doped into the optimized composition $K_7CaGd_2(B_5O_{10})_3$:0.03Tb^{3+}. The photoluminescence (PL) spectra under 377 nm excitation are shown in Fig. 4(a-b) for Li^+ and Na^+ co-doped samples, respectively. The emission profiles remain dominated by the characteristic $^5D_4 \rightarrow {}^7F_J$ ($J = 6$–3) transitions of Tb^{3+}, confirming that the host lattice structure is maintained upon alkali co-doping.

As shown in Fig. 4(a), a gradual increase in PL intensity is observed with increasing Li^+ content, reaching a maximum at $y = 0.03$, beyond which the emission begins to decline due to concentration quenching. This enhancement is attributed to improved charge compensation and reduced nonradiative relaxation via defect passivation by Li^+ ions, which can occupy interstitial sites and locally distort the lattice, thereby strengthening the crystal field around Tb^{3+}.

In contrast, as seen in Fig. 4(b), Na^+ co-doping also improves the emission intensity up to $y = 0.02$, but the overall enhancement is slightly weaker than that observed for Li^+. This can be explained by the relatively larger ionic radius of Na^+, leading to a less efficient lattice distortion and weaker local field modification. Both Li^+ and Na^+ co-doped samples show no shift in emission wavelength, indicating that the local site symmetry of Tb^{3+} remains largely unchanged. The differences between Li^+ and Na^+ co-doping can be understood from their ionic radii and lattice interaction behavior. The smaller Li^+ ion (0.76 Å) can more easily occupy interstitial or substituted sites, generating stronger local lattice distortion and more effective charge compensation around Tb^{3+} centers. This is consistent with the slightly sharper XRD peaks and higher PL intensities observed for Li^+-co-doped samples. In contrast, the larger Na^+ ion (1.02 Å) induces weaker distortion and leaves a greater density of residual defects, which is reflected in its lower thermal stability and smaller enhancement in PL emission. These structural differences provide spectroscopic evidence for the superior efficiency of Li^+ in passivating defects and enhancing radiative recombination in the KCGBO host.

These results demonstrate that alkali-ion co-doping can effectively modulate luminescence intensity through microstructural and electronic effects without altering the Tb^{3+} emission mechanism, with Li^+ proving to be the more efficient charge compensator in the KCGBO host.

4.3. Thermal quenching behavior and activation energy analysis

The temperature-dependent photoluminescence (PL) behavior of the KCGBO:0.03Tb^{3+}, KCGBO:0.03Tb^{3+},0.03Li^+, and KCGBO:0.03 Tb^{3+},0.02Na^+ phosphors in the range of 300–550 K is shown in Fig. 5a-c. The temperature-dependent normalised photoluminescence (PL) behavior of the KCGBO:0.03Tb^{3+}, KCGBO:0.03Tb^{3+},0.03Li^+, and KCGBO:0.03Tb^{3+},0.02Na^+ phosphors in the range of 300–550 K is shown in Fig. 5(d–f). All samples exhibit the characteristic emission transitions of Tb^{3+} ions arising from the $^5D_4 \rightarrow {}^7F_J$ ($J = 6$–3) manifold, with a prominent green band at 542 nm and a weak red band around 670 nm.

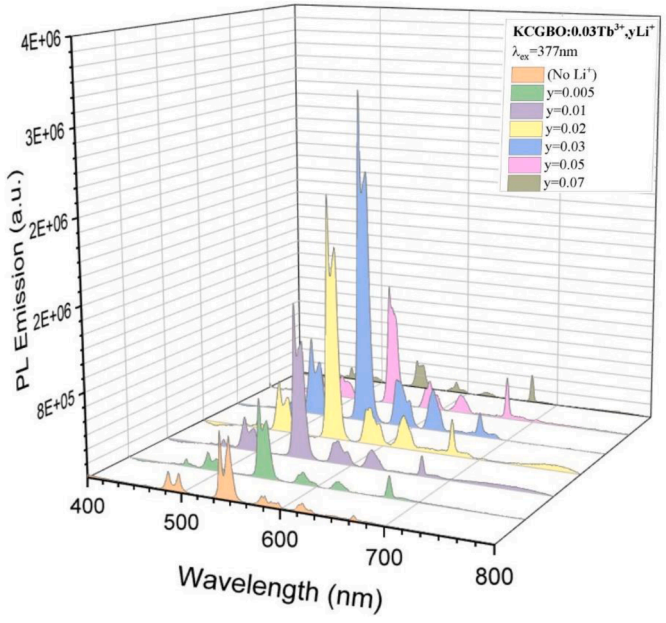

(a)

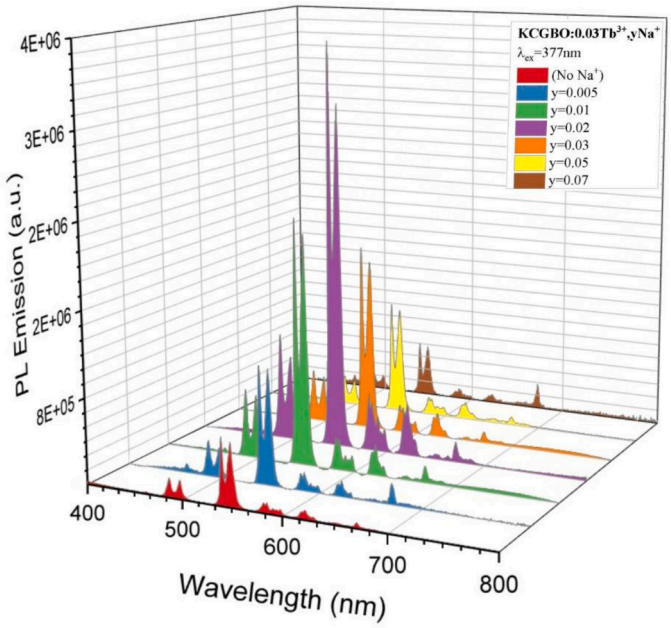

(b)

Fig. 4. (a) PL spectra of KCGBO:0.03Tb^{3+},yLi^{+} and (b) KCGBO:0.03Tb^{3+},yNa^{+} under 377 nm excitation.

The overall emission intensity decreases gradually with increasing temperature up to ~430–450 K, indicating thermal quenching of luminescence. Above this temperature, a partial recovery of PL intensity is observed, especially for the 670 nm line, suggesting thermally stimulated carrier release from shallow traps that repopulate the $^5D_4$ excited state. This phenomenon, often termed *anti-thermal quenching*, has been reported in oxide hosts, including borates, phosphates, and niobates [38, 39]. These shallow traps are frequently reported in borate-based phosphors and are generally associated with defect-related states induced by lattice distortion and charge-compensation effects. Such defects introduce energy levels a few tenths of an electron volt below the conduction band, enabling them to capture photoexcited carriers at low temperatures. Upon heating, their activation energy becomes comparable to *kT*, leading to thermally stimulated detrapping of electrons that subsequently feed the Tb^{3+} $^5D_4$ level. This process provides an additional radiative recombination pathway and explains the observed partial recovery of emission intensity at elevated temperatures—a mechanism widely reported in borate-based phosphors. The observed enhancement at elevated temperatures can be associated with thermally activated defect-related processes that facilitate energy transfer to Tb^{3+} ions, leading to a transient increase in emission intensity, as commonly reported in Tb^{3+}-doped glass systems [25]. A similar thermally activated detrapping mechanism was also observed by Hakami et al. [33]in rare-earth-doped borate hosts, confirming that shallow trap-assisted

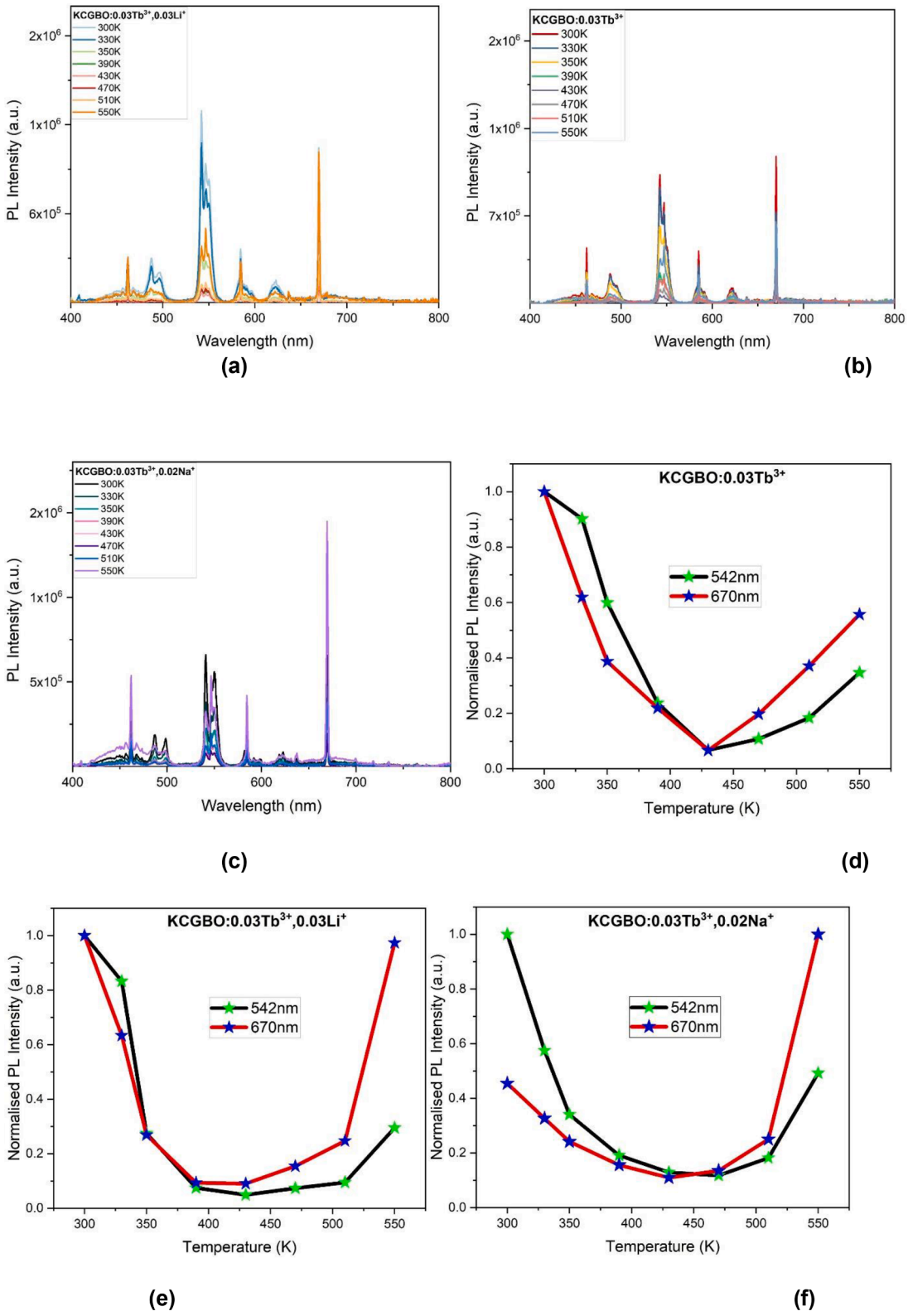

Fig. 5. (a–c) Temperature-dependent PL emission spectra of KCGBO:0.03Tb^{3+}, KCGBO:0.03Tb^{3+},0.03Li^{+}, and KCGBO:0.03Tb^{3+},0.02Na^{+} phosphors measured in the 300–550 K range under 377 nm excitation. (d–f) normalized PL intensity variations at 542 nm and 670 nm as a function of temperature, illustrating the thermal quenching and anti-thermal quenching behavior of the samples.

energy feedback can cause emission recovery at high temperatures.

The thermal quenching process can be described by the Arrhenius relation [1,24]:

$$I(T) = \frac{I_0}{1 + Cexp(-E_a/k_BT)} \quad (5)$$

where $I(T)$ and I_0 are the PL intensities at temperature T and room temperature, respectively, C is a constant, k_B is Boltzmann's constant, and E_a is the activation energy required to thermally activate non-radiative pathways. By rearranging this equation into a linearized form,

$$ln\left[\frac{I_o}{I(T)} - 1\right] = lnC - \frac{E_a}{k_BT} \quad (6)$$

the slope of the linear fit to $ln\left[\frac{I_o}{I(T)} - 1\right]$ versus $1/k_BT$ provides the value of E_a. The corresponding Arrhenius plots for the three compositions are displayed in Fig. 6 (a-c).

The calculated activation energies are 0.55 eV for KCGBO:0.03Tb^{3+}, 0.52 eV for KCGBO:0.03Tb^{3+},0.03Li^{+}, and 0.25 eV for KCGBO:0.03Tb^{3+},0.02Na^{+}. Although direct defect-sensitive spectroscopic techniques (e.g., EPR or thermoluminescence) are beyond the scope of the present study, the origin of the shallow traps responsible for the anti-thermal-quenching behavior can be rationalized within a crystal-chemical framework. From a crystal-chemical perspective, the pronounced difference in activation energies observed for Li^{+}- and Na^{+}-co-doped samples can be understood by considering ionic size mismatch and local lattice relaxation effects.

Li^{+}, with a significantly smaller ionic radius than K^{+}, introduces stronger local lattice strain and more pronounced distortion of the Tb–O coordination environment, which favors the formation of relatively deeper defect-related trap states and results in a higher activation energy for thermal detrapping ($E_a \approx 0.52$ eV). In contrast, the larger Na^{+} ion induces comparatively weaker lattice relaxation, leading to shallower trap levels that require lower thermal energy ($E_a \approx 0.25$ eV). This size-driven defect energetics model offers a consistent mechanistic framework linking alkali-ion incorporation, charge compensation, lattice distortion, and trap depth, even in the absence of direct defect spectroscopic measurements.

In contrast, the smaller E_a for Na^{+}-co-doped phosphor suggests more efficient thermal energy transfer to quenching centers, resulting in faster luminescence decay with temperature.

The improvement in thermal stability with Li^{+} incorporation can be ascribed to several synergistic effects. First, Li^{+} acts as an effective

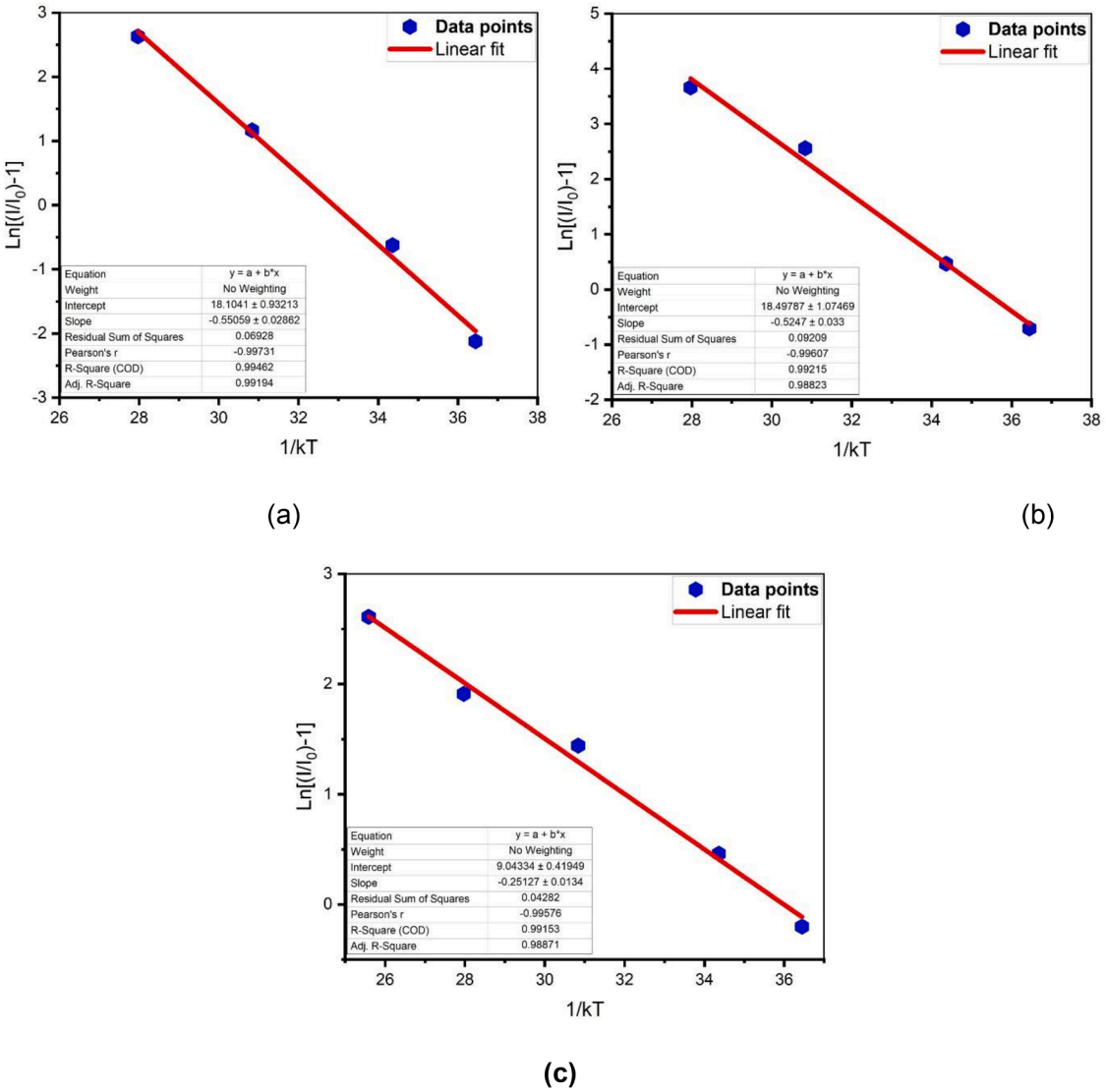

Fig. 6. Arrhenius plots of ln[$(I_o/I)-1$] versus $1/kT$ for (a) KCGBO:0.03Tb^{3+}, (b) KCGBO:0.03Tb^{3+},0.03Li^{+}, and (c) KCGBO:0.03Tb^{3+},0.02Na^{+} phosphors. linear fits were used to determine activation energy (ΔE) values indicating thermal quenching behavior.

charge compensator for Tb^{3+} incorporation into the KCGBO lattice, reducing defect-induced nonradiative centers [25]. Second, Li^+ may introduce shallow traps within the bandgap, which serve as temporary reservoirs for photoexcited carriers. Upon heating, these carriers are thermally released and transferred back to the Tb^{3+} $^5D_4$ level, thereby enhancing emission at higher temperatures—a mechanism consistent with the observed anti-thermal quenching trend [1]. The order of activation energies (Li^+-co-doped > undoped > Na^+-co-doped, where the undoped sample refers to the Tb^{3+}-doped $K_7CaGd_2(B_5O_{10})_3$ without Li^+/Na^+ co-doping) directly correlates with the observed high-temperature PL retention, confirming that Li^+ co-doping effectively enhances the thermal robustness of the host lattice. Such activation energy values (≈ 0.3–0.5 eV) are consistent with those typically reported for thermally stable Tb^{3+}-doped borate and tungstate phosphors [40]. These activation energy values also provide insights into the defect environment and lattice dynamics. E_a values in the range of 0.3–0.6 eV are frequently reported for borate-based phosphors exhibiting thermally activated defect-related processes, reflecting the involvement of shallow-to-moderate trap states arising from lattice distortion and charge-compensation effects. A higher E_a indicates that stronger phonon coupling or deeper defect states are required to activate quenching pathways, thereby improving the thermal stability of the phosphor. Conversely, the lower E_a observed for the Na^+-co-doped sample suggests a closer energetic proximity between defect states and the Tb^{3+} excited levels, allowing lattice vibrations to more easily trigger nonradiative relaxation. Thus, the differences in E_a reflect the interplay between defect structure, phonon interactions, and the overall thermal quenching resistance of the host lattice.

Overall, the results indicate that Li^+ co-doped KCGBO:Tb^{3+} phosphors exhibit the most efficient suppression of nonradiative relaxation and thus the best thermal stability among the investigated compositions. These features make Li^+-modified KCGBO:Tb^{3+} a promising candidate for thermally resilient, near-UV-excitable green phosphors suitable for high-power solid-state ligting applications.

4.4. Lifetime analysis

The luminescence decay profiles of KCGBO:Tb^{3+} and co-doped phosphors were recorded under 377 nm excitation and are depicted in Fig. 7. All decay curves exhibit a non-single exponential behavior, indicating the presence of multiple radiative and non-radiative recombination pathways. Therefore, the experimental data were fitted using a tri-exponential function of the form

$$I(t) = A_1 e^{-t/\tau_1} + A_2 e^{-t/\tau_2} + A_3 e^{-t/\tau_3} \quad (7)$$

where A_i and τ_i $(i = 1–3)$ represent the pre-exponential constants and the corresponding decay components, respectively. The average lifetime (τ_{avg}) was calculated using the relation

$$\tau_{avg} = \frac{\sum A_i \tau_i^2}{\sum A_i \tau_i} \quad (8)$$

The derived lifetime parameters are summarized in Table 5. For the undoped series, the average lifetime initially increased with Tb^{3+} concentration, reaching a maximum value of 1122 μs for KCGBO:0.03Tb^{3+}, followed by a decrease to 714 μs at higher doping (0.05 Tb^{3+}). This concentration-dependent behavior is attributed to the well-known *concentration quenching effect*, where excessive activator ions enhance cross-relaxation and energy migration among Tb^{3+} centers, thereby promoting non-radiative decay channels.

When co-doped with Li^+ and Na^+ ions, distinct variations in decay dynamics were observed. The incorporation of Li^+ ions notably prolonged the average lifetime to 1743 μs for KCGBO:0.03Tb^{3+},0.05Li^+, signifying a reduced non-radiative recombination rate. This enhancement can be associated with local charge compensation and the stabilization of crystal field symmetry around Tb^{3+} ions. The introduction of Li^+ likely facilitates substitution at K^+ sites due to its comparable ionic radius, leading to improved energy transfer efficiency and suppression of quenching centers. In contrast, Na^+ co-doping yielded shorter lifetimes (660–724 μs), implying that Na^+ perturbs the local symmetry less

Table 5
Lifetime parameters (τ_1, τ_2, τ_3), relative contributions, average lifetime (τ_{avg}), and χ^2 values for KCGBO:Tb^{3+} and co-doped samples.

		Time(μs)	Rel. %	τ_{avg} (μs)	χ^2
KCGBO:0.01Tb^{3+}	τ_1	12.396	50.34	779.796	1.1039
	τ_2	779.804	49.66		
KCGBO:0.03Tb^{3+}	τ_1	9.616	32.17	1122.494	1.0175
	τ_2	439.872	33.93		
	τ_3	1912.112	33.90		
KCGBO: 0.05Tb^{3+}	τ_1	12.632	53.25	714.186	1.0875
	τ_2	794.076	46.75		
KCGBO:0.03Tb^{3+},0.03Li^+	τ_1	12.300	40.60	1055.648	1.2139
	τ_2	427.220	26.95		
	τ_3	1707.820	32.45		
KCGBO:0.03Tb^{3+},0.05Li^+	τ_1	10.956	31.08	1743.616	1.1495
	τ_2	492.728	31.72		
	τ_3	2955.604	37.20		
KCGBO:0.03Tb^{3+},0.02Na^+	τ_1	12.756	51.04	724.373	1.0133
	τ_2	798.532	48.96		
KCGBO:0.03Tb^{3+},0.05Na^+	τ_1	11.756	49.81	660.087	1.0009
	τ_2	724.424	50.19		

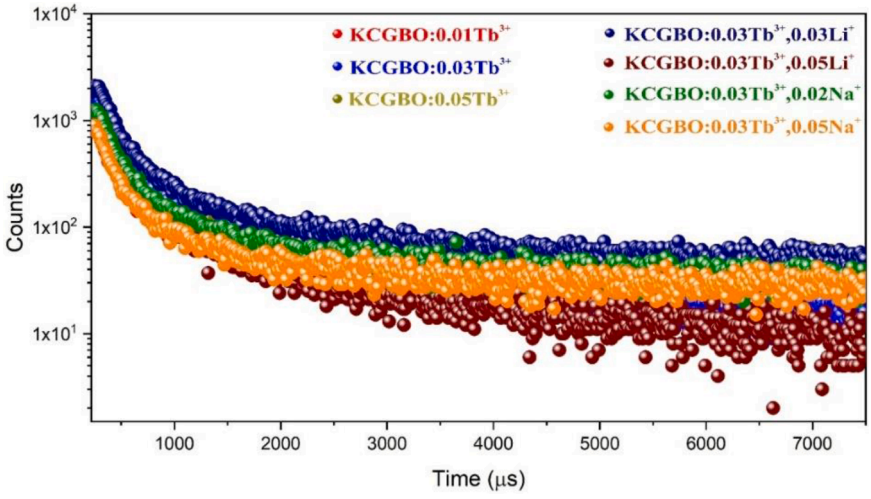

Fig. 7. Decay profiles of KCGBO:Tb^{3+} and co-doped phosphors under 377 nm excitation showing multi-exponential behavior.

effectively than Li^+ and may introduce competing relaxation channels. The fitting quality, confirmed by χ^2 values ranging from 1.00 to 1.21, demonstrates excellent agreement between experimental and simulated curves. These findings reveal that Li^+ co-doping significantly enhances radiative recombination probability, whereas Na^+ co-doping shows a moderate or even detrimental effect on the persistence of Tb^{3+} emission. Consequently, Li^+ emerges as a more efficient charge compensator for optimizing the afterglow characteristics of KCGBO:Tb^{3+} phosphors.

4.5. Radiative parameters derived from Judd–Ofelt analysis for the $^5D_4 \rightarrow {}^7F_5$ transition of Tb^{3+} in KCGBO phosphors co-doped with Li^+ and Na^+

Although Judd–Ofelt (J–O) analysis is traditionally applied to ions with predominantly electric-dipole (ED) transitions such as Eu^{3+}, Er^{3+}, or Dy^{3+}, its application to Tb^{3+} requires clarification because the $^5D_4 \rightarrow {}^7F_j$ manifold includes strong magnetic-dipole (MD) contributions. However, in non-centrosymmetric hosts such as KCGBO (space group R32), several Tb^{3+} transitions acquire measurable ED character. Therefore, in the present work only ED-allowed or mixed ED–MD transitions were used in the fitting, while purely MD transitions (e.g., $^5D_4 \rightarrow {}^7F_6$) were excluded. Accordingly, the extracted Ω_2, Ω_4, and Ω_6 parameters are interpreted in a comparative rather than absolute sense, enabling reliable assessment of how Li^+/Na^+ co-doping modifies the local symmetry and radiative probability of Tb^{3+} sites.

To understand the radiative behavior of Tb^{3+} ions in the KCGBO phosphor matrix, Judd–Ofelt (J–O) theory was applied to analyze the photoluminescence emission spectra. Although originally developed for rare-earth ions such as Eu^{3+} with $^5D_0 \rightarrow {}^7F_J$ transitions, the J–O formalism can also be adapted to Tb^{3+}, whose $^5D_4 \rightarrow {}^7F_J$ (J = 6–3) transitions include both electric and magnetic dipole contributions. In this context, the $^5D_4 \rightarrow {}^7F_5$ transition, typically the most intense emission for Tb^{3+}, is used as a reference for calculating radiative properties. Due to the mixed dipole nature of these transitions, direct extraction of J–O intensity parameters (Ω_2, Ω_4, Ω_6) is not standard for Tb^{3+} systems. Instead, radiative parameters such as the spontaneous emission probability (A_J), radiative lifetime (τ_{rad}), branching ratio (β_r), and optical gain (G) are calculated using integrated emission intensities and theoretical line strength values.

The expressions for the electric-dipole line strength, spontaneous emission probability, radiative decay rate, radiative lifetime, and branching ratio follow the standard Judd–Ofelt formalism originally developed by Judd [16] and Ofelt [17], with reduced matrix elements adopted from Carnall et al. [41]. Modern implementations of the method were consulted from Hovhannisyan et al. [42] and Liu et al. [43].

The J–O intensity parameters were determined by fitting the experimental oscillator strengths (f_{exp}) to the theoretical expression for electric dipole transitions. The spontaneous emission probability A_J for each transition was calculated using:

$$A_J = \frac{64\pi^4 e^2}{3h\lambda^3(2J+1)} \cdot n\left(n^2+2\right)^2 \cdot \frac{S_{ed}}{9} \tag{9}$$

where λ is the emission wavelength, n is the refractive index of the host (assumed as 1.5), and S_{ed} is the electric dipole line strength, which is linearly related to the intensity parameters:

$$S_{ed} = \sum_{t=2,4,6} \Omega_t \left| \langle {}^5D_4 \parallel U^{(t)} \parallel {}^7F_J \rangle \right|^2 \tag{10}$$

Reduced matrix elements $^5D_0 \| U^{(t)} \| {}^7F_J$ are fixed values for Eu^{3+} and were taken from Carnall's tabulations. Reduced matrix elements $\langle U(\lambda) \rangle^2$ were adopted from free-ion tabulated values reported by Carnall et al., as commonly employed in adapted Judd–Ofelt analyses of Tb^{3+} ions in non-centrosymmetric fluoride and borate hosts, where the extracted intensity parameters are interpreted in a comparative rather than absolute sense [44,45]. Although Eu^{3+}-based reduced matrix elements are employed, their use for Tb^{3+} transitions is justified by the similar 4f–4f transition framework and has been widely adopted in comparative Judd–Ofelt analyses of Tb^{3+}-activated non-centrosymmetric fluoride and borate hosts. Consistent with previous reports, the radiative parameters derived using an adapted Judd–Ofelt formalism in the present work—such as the spontaneous emission probability, radiative lifetime, and stimulated emission cross-section—are of the same order of magnitude as those reported for Tb^{3+} in fluoride and borate host lattices. Once the emission probabilities were obtained, additional radiative properties were derived. The branching ratio of the $^5D_0 \rightarrow {}^7F_2$ transition, representing the fraction of radiative decay through this channel, was calculated using:

$$\beta_r = \frac{A_J}{\sum A_J} \tag{11}$$

The radiative lifetime τ_{rad} was estimated as:

$$\tau_{rad} = \frac{1}{\sum A_J} \tag{12}$$

and compared to the experimental lifetime τ_{exp} (obtained from time-resolved decay measurements), the non-radiative decay rate W_{NR} was extracted as:

$$W_{NR} = \frac{1}{\tau_{exp}} - \frac{1}{\tau_{rad}} \tag{13}$$

To further evaluate the emission efficiency, the stimulated emission cross-section σ and optical gain G were calculated using:

$$\sigma = \frac{\lambda^4 A_J}{8\pi n^2 c \tau_{exp}}, \quad G = \beta_r \cdot \sigma \tag{14}$$

Building on the radiative analysis framework, Judd–Ofelt-derived parameters were obtained for the $^5D_4 \rightarrow {}^7F_5$ transition of Tb^{3+} in KCGBO phosphors co-doped with Li^+ and Na^+. Judd–Ofelt intensity parameters and corresponding radiative properties were also evaluated for the $^5D_4 \rightarrow {}^7F_5$ transition of Tb^{3+} ions in KCGBO:0.03Tb^{3+} and its Li^+/Na^+ co-doped derivatives. The calculated spontaneous emission probability A_J increased significantly upon Li^+ and Na^+ incorporation, indicating an enhanced electric dipole contribution as a result of the local symmetry distortion introduced by alkali ions. The branching ratio β_r rose from 0.28 (Tb^{3+} doped) to 0.34 (Li^+) and 0.33 (Na^+), suggesting more efficient emission via the green $^5D_4 \rightarrow {}^7F_5$ channel. Radiative lifetimes τ_{rad} decreased with co-doping, consistent with increased transition probabilities. The good agreement between calculated and experimental lifetimes confirms the internal consistency of the Judd–Ofelt fitting despite the partial magnetic-dipole character of Tb^{3+} transitions. This consistency further supports the presence of measurable electric-dipole contributions induced by the local symmetry distortion of the Tb^{3+} sites. This interpretation is also consistent with the dominance of the $^5D_4 \rightarrow {}^7F_5$ emission band over the nominally magnetic-dipole-allowed $^5D_4 \rightarrow {}^7F_6$ transition observed in the photoluminescence spectra. Additional evidence is provided by the photoluminescence spectra (Fig. 3), where the integrated intensity of the hypersensitive $^5D_4 \rightarrow {}^7F_5$ transition is markedly higher than that of the predominantly magnetic-dipole $^5D_4 \rightarrow {}^7F_6$ transition, providing clear spectral evidence for enhanced electric-dipole contributions induced by local symmetry distortion. Optical gain values were also enhanced ($G = 1.08 \times 10^{-22}$ cm^2 for Li^+), indicating a clear improvement in emission performance due to co-doping. The corresponding radiative parameters are summarized in Table 6. For comparison, previous Judd–Ofelt-based studies on Tb^{3+}-activated fluoride and borate systems [44,45] report spontaneous emission probabilities, radiative lifetimes, and stimulated emission cross-sections within similar ranges. In particular, the radiative parameters derived in the present work—such as the spontaneous emission probability, radiative lifetime, branching ratio, and stimulated emission cross-section for the $^5D_4 \rightarrow {}^7F_5$ transition—fall within the typical range and are of the same

Table 6
Radiative properties for the $^5D_4 \rightarrow {}^7F_5$ transition of Tb^{3+} in KCGBO samples with and without alkali co-doping.

Composition	A_J (s^{-1})	β_r	τ_{rad} (ms)	τ_{exp} (ms)	W_{NR} (s^{-1})	σ ($\times 10^{-22}$ cm^2)	Optical gain ($\times 10^{-22}$ cm^2)
KCGBO:0.03Tb^{3+}	6.23×10^5	0.28	0.160	1.342	5.93×10^3	2.14	0.60
KCGBO:0.03Tb^{3+},0.03Li^+	1.12×10^6	0.34	0.089	1.104	9.36×10^3	3.18	1.08
KCGBO:0.03Tb^{3+},0.03Na^+	9.87×10^5	0.33	0.101	1.202	8.22×10^3	2.94	0.97

order of magnitude as those reported for Tb^{3+} in non-centrosymmetric fluoride and borate host lattices. Overall, this consistency confirms the physical reliability of the adapted Judd–Ofelt radiative analysis applied to the KCGBO phosphor system. These results confirm the beneficial role of alkali co-dopants in optimizing the radiative dynamics and emission efficiency of Tb^{3+}-doped KCGBO phosphors for green light applications.

To indirectly assess the radiative performance of the Tb^{3+}-activated KCGBO phosphors, the intrinsic internal quantum efficiency η_{int} was estimated using the relation $\eta_{int} = \tau_{meas}/\tau_{rad}$, where τ_{meas} is the experimental photoluminescence decay time and τ_{rad} is the radiative lifetime derived from Judd–Ofelt parameters. The calculated efficiencies indicate that the co-doping of Li^+ and Na^+ substantially enhances the

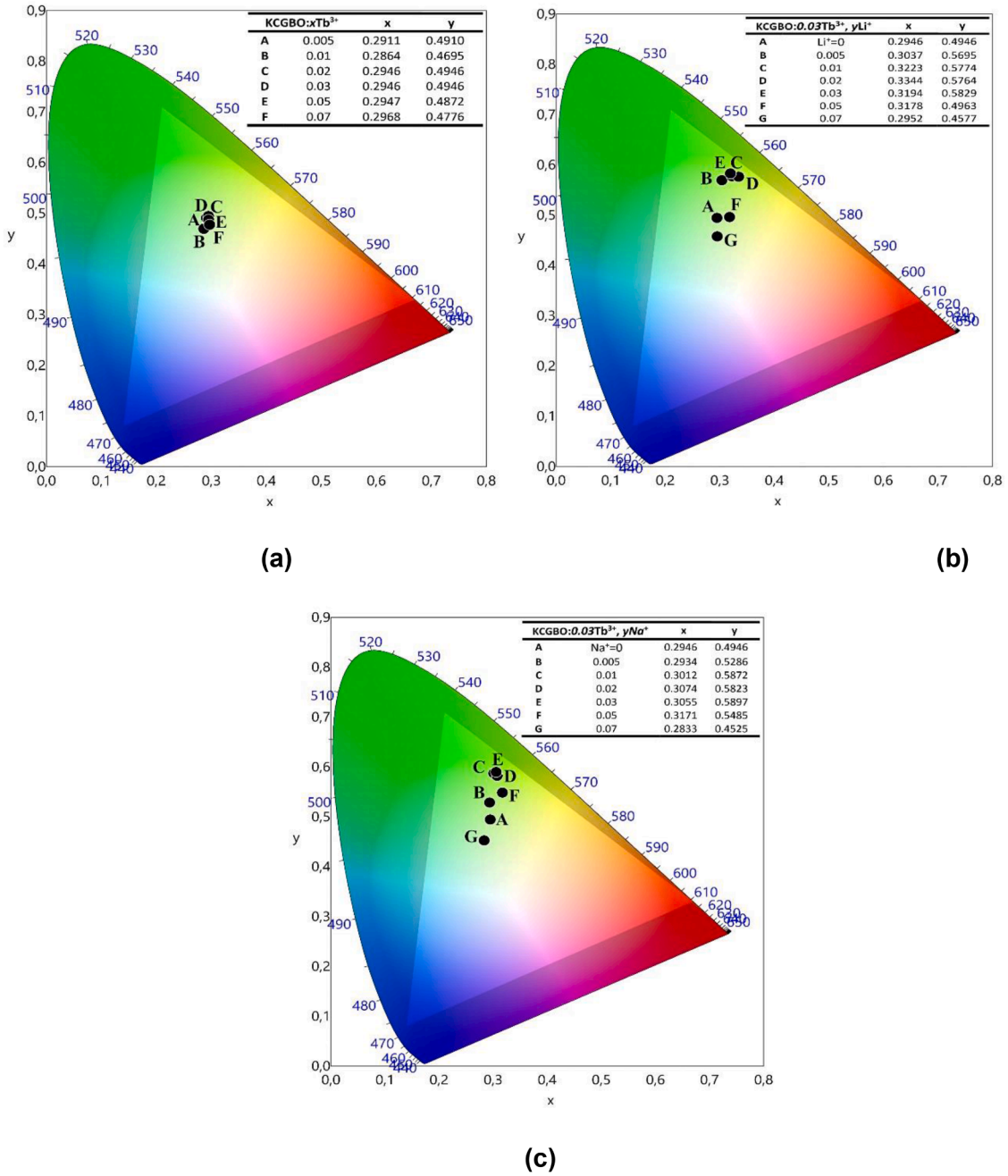

Fig. 8. CIE 1931 chromaticity coordinates for (a) KCGBO:xTb^{3+} (x = 0.005–0.07), (b) KCGBO:0.03Tb^{3+},yLi^+, and (c) KCGBO:0.03Tb^{3+},yNa^+ phosphors; inset values show the calculated coordinates.

radiative output by suppressing non-radiative pathways. Specifically, the intrinsic efficiency increased from 68.6 % for the undoped KCGBO:0.03Tb^{3+} sample to 91.0 % and 88.5 % for the 0.03Li^{+} and 0.03Na^{+} co-doped samples, respectively. These results confirm the effectiveness of alkali ion incorporation in modulating the local crystal field and enhancing the radiative probability of Tb^{3+} transitions.

4.4. CIE chromaticity coordinates and color purity analysis

The CIE 1931 chromaticity diagrams of KCGBO:$x$$Tb^{3+}$, KCGBO:0.03$Tb^{3+}$,$y$$Li^{+}$, and KCGBO:0.03$Tb^{3+}$,$y$$Na^{+}$ phosphors are presented in Fig. 8(a–c), and their corresponding chromaticity coordinates (x, y), correlated color temperature (CCT), and color purity (CP %) values are summarized in Table 6. All compositions exhibit emission coordinates located in the green region of the CIE color space, originating from the characteristic $^5D_4 \rightarrow {}^7F_5$ transition of Tb^{3+} ions at ~542 nm.

With increasing Tb^{3+} concentration, the emission coordinates show only slight variations, indicating good color stability. In contrast, Li^{+} and Na^{+} co-doping induce a noticeable upward shift in the y coordinate, implying enhanced green saturation and color purity. As shown in Table 7, the color purity values increase from ~60 % (undoped) to over 90 % for Li^{+} and Na^{+} co-doped samples, confirming improved chromatic performance. This enhancement is attributed to the charge compensation effect and local lattice distortion introduced by alkali ions, which reduce non-radiative relaxation and improve energy transfer efficiency between Tb^{3+} centers.

Such stable and highly pure green emissions are advantageous for solid-state lighting and display applications, consistent with previous findings on alkali co-doped borate phosphors [8,31,46]. The obtained color purity (up to >90 % for Li^{+} and Na^{+} co-doped samples) is highly relevant for practical solid-state lighting, as high-purity emission minimizes spectral leakage and improves color saturation in green pixels, phosphor-converted LEDs, and display backlights. Moreover, the correlated color temperature (CCT) values in the range of 5100–5800 K fall within the preferred cool-white to daylight illumination range, making these phosphors suitable for high-brightness near-UV-excited LED packages. The combination of high color purity, stable chromaticity coordinates, and CCT values close to standard white-light regions indicates that the KCGBO:Tb^{3+}-based phosphors can deliver efficient and visually consistent green emission for practical lighting and display applications.

5. Conclusions

Li^{+} and Na^{+} co-doped $K_7CaGd_2(B_5O_{10})_3$:Tb^{3+} (KCGBO) phosphors were successfully synthesized via a microwave-assisted combustion route and comprehensively characterized for their structural, optical, and thermal properties. Rietveld refinement confirmed the formation of a single-phase rhombohedral structure (R32), demonstrating the high structural stability of the KCGBO host upon rare-earth and alkali substitution. Complementary FTIR and Raman analyses verified the preservation of the [B_5O_{10}] polyborate framework and confirmed the absence of impurity phases or local distortions induced by co-doping. Photoluminescence studies revealed strong green emission at ~544 nm corresponding to the $^5D_4 \rightarrow {}^7F_5$ transition of Tb^{3+} ions, with optimum intensity at 3 wt % Tb^{3+} concentration. Li^{+}/Na^{+} co-doping further enhanced emission efficiency through charge compensation and local lattice distortion, effectively suppressing non-radiative relaxation. Judd–Ofelt analysis confirmed that Li^{+} co-doping significantly improved radiative parameters, including spontaneous emission probability (A_J), radiative lifetime (τ_{rad}), and optical gain (G), for the $^5D_4 \rightarrow {}^7F_5$ transition. Temperature-dependent PL measurements revealed excellent thermal stability, with the Li^{+}-co-doped sample retaining 82 % of its initial intensity at 450 K and exhibiting an activation energy of ~0.52 eV, indicating trap-assisted carrier detrapping and partial anti-thermal quenching. The superior thermal stability of the Li^{+}-co-doped sample compared to its Na^{+}-co-doped counterpart is attributed to size-induced lattice distortion and charge-compensation effects, which modulate defect-related trap depth and result in a higher activation energy for thermal detrapping. CIE chromaticity analysis showed emission coordinates located in the green region ($x \approx 0.32$, $y \approx 0.58$) with color purity exceeding 90 %, confirming vivid and spectrally stable green emission. Overall, these results demonstrate that Li^{+} co-doping not only enhances the radiative and thermal performance but also improves chromatic stability, establishing KCGBO:Tb^{3+} as a promising green phosphor for near-UV-pumped solid-state lighting and display applications. Although Tb^{3+} transitions involve mixed electric– and magnetic–dipole contributions, the Judd–Ofelt parameters extracted here provide reliable comparative insight into symmetry modification induced by Li^{+}/Na^{+} co-doping.

Table 7
Chromaticity coordinates (x, y), correlated color temperature (CCT), and color purity (CP) % of KCGBO:$x$$Tb^{3+}$, KCGBO:0.03$Tb^{3+}$,$y$$Li^{+}$, and KCGBO:0.03$Tb^{3+}$, $y$$Na^{+}$ phosphors.

Tb^{3+} content (wt. %)	x	y	CCT	Color Purity (CP) %
$x = 0.005$	0.2911	0.4910	6499	61
$x = 0.01$	0.2864	0.4695	6710	54
$x = 0.02$	0.2946	0.4946	6398	62
$x = 0.03$	0.2946	0.4946	6398	62
$x = 0.05$	0.2947	0.4872	6418	59
$x = 0.07$	0.2968	0.4776	6395	56
Li^{+} content (wt. %)	x	y	CCT	Color Purity (CP) %
$y = 0.005$	0.3037	0.5695	6042	89
$y = 0.01$	0.3223	0.5774	5692	91
$y = 0.02$	0.3344	0.5764	5478	91
$y = 0.03$	0.3194	0.5829	5740	94
$y = 0.05$	0.3178	0.4963	5839	61
$y = 0.07$	0.2952	0.4577	6510	49
Na^{+} content (wt. %)	x	y	CCT	Color Purity (CP) %
$y = 0.005$	0.2946	0.4946	6334	62
$y = 0.01$	0.2934	0.5286	6064	75
$y = 0.02$	0.3012	0.5872	5957	96
$y = 0.03$	0.3074	0.5823	5983	94
$y = 0.05$	0.3055	0.5897	5806	97
$y = 0.07$	0.3171	0.5485	6886	81

CRediT authorship contribution statement

S. Yusan: Software, Methodology, Investigation, Funding acquisition. **M.B. Coban:** Software, Methodology, Investigation. **U.H. Kaynar:** Software, Methodology, Investigation, Funding acquisition. **I.G. Kaptanoglu:** Software, Methodology, Investigation. **Abeer S. Altowyan:** Writing – original draft, Methodology, Investigation, Funding acquisition. **Jabir Hakami:** Software, Methodology, Investigation. **H. Aydin:** Software, Methodology, Investigation. **E.E. Karali:** Software, Methodology, Investigation. **A. Canimoglu:** Methodology, Investigation, Conceptualization. **N. Can:** Writing – review & editing, Writing – original draft.

Declaration of competing interest

The authors declare that they have no known competing financial interests or personal relationships that could have appeared to influence the work reported in this paper.

Acknowledgements

We would like to express our sincere gratitude to the Scientific Research Projects Coordination Unit of Ege University (Project Number: 33037), the Princess Nourah bint Abdulrahman University Researchers

Supporting Project (Project No. PNURSP2026R16), Princess Nourah bint Abdulrahman University, Riyadh, Saudi Arabia. This study was also financially supported by the Scientific and Technological Research Council of Turkey (TÜBITAK, Project No. 223M036).

Data availability

Data will be made available on request.

References

[1] P.K. Tawalare, Luminescent inorganic mixed borate phosphors materials for lighting, Luminescence 37 (2022) 1226–1245, https://doi.org/10.1002/bio.4301.
[2] D.P. Awade, BoratePhosphors for solid-state lighting, in: Borate Phosphors, CRC Press, Boca Raton, 2022: pp. 75–106. https://doi.org/10.1201/9781003207757-4.
[3] A.S. Altowyan, U.H. Kaynar, C. Gök, H. Aydin, J. Hakami, M.B. Coban, A. Canimoglu, N. Can, Photoluminescence characteristics and Judd–Ofelt analysis of $YBa_3(BO_3)_3$:tb^{3+} phosphors co-doped with Li^+, Na^+, and K^+, J. Lumin. 286 (2025) 121380 https://doi.org/10.1016/j.jlumin.2025.121380.
[4] Z. Xie, Y. Wang, S. Cheng, G. Han, Z. Yang, S. Pan, Synthesis, characterization, and theoretical analysis of three new nonlinear optical materials $K_7MRE_2B_{15}O_{30}$ (M= Ca and Ba, RE= La and Bi), Sci. China Mater. 62 (2019) 1151–1161, https://doi.org/10.1007/s40843-019-9412-5.
[5] A.B. Kuznetsov, D.M. Ezhov, K.A. Kokh, N.G. Kononova, V.S. Shevchenko, B. Uralbekov, A. Bolatov, V.A. Svetlichnyi, I.N. Lapin, E.A. Simonova, A.E. Kokh, Nonlinear optical crystals $K_7CaR_2(B_5O_{10})_3$ (R = Nd, Yb), growth and properties, J. Cryst. Growth 519 (2019) 54–59, https://doi.org/10.1016/j.jcrysgro.2019.05.007.
[6] X. Gao, Q. Liu, Z. Yang, J. Han, S. Pan, $Rb_7PbY_2(B_5O_{10})_3$: a noncentrosymmetric rare-earth borate nonlinear optical crystal with $[B_5O_{10}]$ unit, Inorg. Chem. 64 (2025) 5821–5826, https://doi.org/10.1021/acs.inorgchem.5c00427.
[7] X. Zhou, C. Yang, S. Liu, Y. Wang, R. Hu, Q. You, W. Liu, M. Liu, S. Yang, X. Jiang, Enhanced photoluminescence of $K_7CaY_2(B_5O_{10})_3$:eu^{3+},Sm^{3+}/Gd^{3+} phosphors through energy transfer and their applications in LED lights for plant growth, J. Alloys Compd. 969 (2023) 172471, https://doi.org/10.1016/j.jallcom.2023.172471.
[8] M.B. Coban, U.H. Kaynar, A.S. Altowyan, J. Hakami, H. Aydin, A. Canimoglu, N. Can, Judd–Ofelt analysis and negative thermal quenching behavior of Tb^{3+}-activated $Ca_3La_3(BO_3)_5$ phosphors co-doped with alkali ions for high-temperature photonic applications, Sens. Actuators A Phys. 395 (2025) 117109, https://doi.org/10.1016/j.sna.2025.117109.
[9] G. Souadi, M.B. Coban, U.H. Kaynar, H. Aydin, S.C. Kaynar, V. Onar, A. Canimoglu, H.J. Alathlawi, N. Can, Structural and luminescence properties of Tb^{3+}-doped $Na_2Gd_2B_2O_7$ phosphors for LED applications: judd–Ofelt analysis and alkali co-doping effects, J. Ind. Eng. Chem. 153 (2026) 742–758, https://doi.org/10.1016/j.jiec.2025.07.037.
[10] A.T. Hines, G. Morrison, B.J. Yarbrough, N.B. Shustova, L.G. Jacobsohn, H.C. zur Loye, Luminescence of alkali rare earth borates $A_3Ln(BO_3)_2$ (A = Na, K; Ln = Eu, Tb), Solid State Sci. 138 (2023) 107130, https://doi.org/10.1016/j.solidstatesciences.2023.107130.
[11] H. Orucu, A.S. Altowyan, U.H. Kaynar, H. Aydin, M.B. Coban, J. Hakami, N. Can, Synthesis, structural characterization, and photoluminescence behavior of $NaCa_4(BO_3)_3$:tb^{3+} phosphors Co-doped with K+: insights into radiation-induced defect formation and charge compensation via DFT calculations, Appl. Radiat. Isot. 225 (2025) 112038, https://doi.org/10.1016/j.apradiso.2025.112038.
[12] A.A. Alsam, U.H. Kaynar, H. Aydin, M.B. Coban, A. Canimoglu, N. Can, Enhanced luminescence and quenching mechanisms in Na^+ Co-doped $K_7CaY_2(B_5O_{10})_3$:tb3+ phosphors under UV radiation, Appl. Radiat. Isot. 217 (2025) 111635, https://doi.org/10.1016/j.apradiso.2024.111635.
[13] L. You, H. Guo, Q. Lu, J. Xie, D. Wu, Z. Chen, G. Zhou, Fluorescent materials of Sm3 + and Tb^{3+} Co-doped $Sr_3B_2O_6$: synthesis and optical properties, Ceram. Int. 51 (2025) 28848–28857, https://doi.org/10.1016/j.ceramint.2025.04.094.
[14] R. Guo, S. Tang, S. Zhong, L. Luo, B. Cheng, Y. Xiong, Photoluminescence properties of $Sr_2MgB_2O_6$:eu^{3+} red phosphor under near-UV excitation, Solid State Sci. 50 (2015) 65–68, https://doi.org/10.1016/j.solidstatesciences.2015.10.012.
[15] N.S. Bajaj, S.K. Omanwar, Combustion synthesis and luminescence characteristics of $NaSr_4(BO_3)_3$:tb^{3+}, J. Lumin. 148 (2014) 169–173, https://doi.org/10.1016/j.jlumin.2013.12.034.
[16] B.R. Judd, Optical absorption intensities of rare-earth ions, Phys. Rev. 127 (1962) 750–761, https://doi.org/10.1103/PhysRev.127.750.
[17] G.S. Ofelt, Intensities of crystal spectra of rare-earth ions, J. Chem. Phys. 37 (1962) 511–520, https://doi.org/10.1063/1.1701366.
[18] A.R. West, Solid State Chemistry and Its Applications, 2nd ed, Wiley, 2022.
[19] R.D. Shannon, Revised effective ionic radii and systematic studies of interatomic distances in halides and chalcogenides, Acta Crystallogr. Sect. A 32 (1976) 751–767, https://doi.org/10.1107/S0567739476001551.
[20] D. Nath, F. Singh, R. Das, X-ray diffraction analysis by Williamson-Hall, Halder-Wagner and size-strain plot methods of CdSe nanoparticles- a comparative study, Mater. Chem. Phys. 239 (2020) 122021, https://doi.org/10.1016/j.matchemphys.2019.122021.
[21] K. Terashima, S. Tamura, S. Kim, T. Yoko, Structure and nonlinear optical properties of lanthanide borate glasses, J. Am. Ceram. Soc. 80 (1997) 2903–2909, https://doi.org/10.1111/j.1151-2916.1997.tb03210.x.
[22] M.A. Morsy, T.F. Garrison, M.R. Kessler, M.H.A. Mhareb, H.Z. El-Deen, Structural elucidation of lithium borate glasses using XRD, FTIR, and EPR spectroscopy, ACS Phys. Chem. Au 5 (2025) 227–238, https://doi.org/10.1021/acsphyschemau.4c00106.
[23] N.D. Ton, N.T. Luan, J.Y. Cho, E.J. Choi, D.W. Jeong, D.J. Daniel, H.J. Kim, S. Kothan, J. Kaewkhao, Comparative study on scintillation and luminescence of Terbium-doped LaB3O6 crystalline and glass materials, J. Lumin. 288 (2025) 121510, https://doi.org/10.1016/j.jlumin.2025.121510.
[24] G. Lakshminarayana, S. Buddhudu, Spectral analysis of Eu^{3+} and Tb^{3+}: b_2O_3–ZnO–PbO glasses, Mater. Chem. Phys. 102 (2007) 181–186, https://doi.org/10.1016/j.matchemphys.2006.11.020.
[25] K. Linganna, S. Ju, C. Basavapoornima, V. Venkatramu, C.K. Jayasankar, Luminescence and decay characteristics of Tb^{3+} -doped fluorophosphate glasses, J. Asian Ceram. Soc. 6 (2018) 82–87, https://doi.org/10.1080/21870764.2018.1442674.
[26] Z. Wan, D. Xu, W. She, F. Xie, Y. Feng, J. Yang, G. Liu, X. Tong, Doping level dependence of the structure and luminescence properties of $LaBO_3$:tb^{3+} phosphors, Ceram. Int. 50 (2024) 9499–9509, https://doi.org/10.1016/j.ceramint.2023.12.268.
[27] K. Jakhar, H. Om, Ca9Al(PO4)7:tb3+—crystal configuration and judd–ofelt modelling of green emanating nanophosphor, Appl. Phys. A 129 (2023) 41, https://doi.org/10.1007/s00339-022-06324-z.
[28] S.C. Kaynar, A.S. Altowyan, H. Aydin, U.H. Kaynar, M.B. Coban, J. Hakami, N. Can, Judd–Ofelt analysis and photoluminescence behavior of Tb^{3+}-activated $K_7SrY_2(B_5O_{10})_3$ phosphors modified with alkali co-dopants for solid-state lighting applications, Spectrochim. Acta Part A Mol. Biomol. Spectrosc. 341 (2025) 126435, https://doi.org/10.1016/j.saa.2025.126435.
[29] G. Blasse, B.C. Grabmaier, Luminescent Materials, Springer Berlin Heidelberg, Berlin, Heidelberg, 1994, https://doi.org/10.1007/978-3-642-79017-1.
[30] R. Reisfield, in: P. Hemm (Ed.), Luminescence of Lanthanides in solids: Excitation processes and Mechanisms, Springer-Verlag, 1987.
[31] S. Verma, K. Verma, D. Kumar, B. Chaudhary, S. Som, V. Sharma, V. Kumar, H. C. Swart, Recent advances in rare earth doped alkali-alkaline earth borates for solid state lighting applications, Phys. B Condens. Matter 535 (2018) 106–113, https://doi.org/10.1016/j.physb.2017.06.073.
[32] W. Xiang, P. Du, J.S. Yu, Synthesis and photoluminescence properties of Tb^{3+}-doped $NaKGdTaO_5$ green-emitting phosphors for information encryption, J. Alloys Compd. 1036 (2025) 181899, https://doi.org/10.1016/j.jallcom.2025.181899.
[33] J. Hakami, Ü.H. Kaynar, M. Ayvacikli, M.B. Coban, J. Garcia-Guinea, P. D. Townsend, M. Oglakci, N. Can, Structural and temperature-dependent luminescence of Terbium doped $YAl_3(BO_3)_4$ phosphor synthesized by the combustion method, Ceram. Int. 48 (2022) 32256–32265, https://doi.org/10.1016/j.ceramint.2022.07.167.
[34] W. Xiang, J.S. Yu, Multi-channel lifetime thermometry and security films based on Ln (Ln = Sm^{3+}, Tb^{3+}, and Sm^{3+}/Tb^{3+}) doped $NaKLaNbO_5$ phosphors, Opt. Laser Technol. 180 (2025) 111450, https://doi.org/10.1016/j.optlastec.2024.111450.
[35] B. Bai, P. Dang, Z. Zhu, H. Lian, J. Lin, Broadband near-infrared emission of $La_3Ga_5GeO_{14}$:tb^{3+},Cr^{3+} phosphors: energy transfer, persistent luminescence and application in NIR light-emitting diodes, J. Mater. Chem. C 8 (2020) 11760–11770, https://doi.org/10.1039/D0TC02498H.
[36] X. Geng, Y. Xie, X. Hu, X. Ouyang, S. Chen, X. Yao, J. Kong, J. Chen, J. Guo, H. Wang, W. Zhou, R. Yu, Greatly enhanced deep-red luminescence performance of Ca_2InSbO_6:mn^{4+} phosphor via multiple optimization strategies, Mater. Today Chem. 26 (2022) 101006, https://doi.org/10.1016/j.mtchem.2022.101006.
[37] D. Zhao, S.-R. Zhang, Y.P. Fan, B.Z. Liu, R.J. Zhang, Thermally stable phosphor $KBa_2(PO_3)_5$:eu^{2+} with broad-band cyan emission caused by multisite occupancy of Eu 2+, Inorg. Chem. 59 (2020) 8789–8799, https://doi.org/10.1021/acs.inorgchem.0c00428.
[38] J. Song, W. Li, H. Cao, Y. Yuan, Y. Cui, N. Guo, Enhancing antithermal quenching in $YTa_{1-x}Nb_xO_4$:tb^{3+} phosphor based on excitation driving and energy transfer, Inorg. Chem. 64 (2025) 18009–18016, https://doi.org/10.1021/acs.inorgchem.5c03338.
[39] R. Xiao, N. Guo, S. Qu, D. Hu, Y. Xin, W. Lv, R. Ouyang, Enhancing antithermal-quenching properties of terbium-doped phosphors through Nb/Ta substitution: insights into the role of intervalence charge transfer and excitation-driven modulation, Ceram. Int. 50 (2024) 28257–28265, https://doi.org/10.1016/j.ceramint.2024.05.125.

[40] P. Dorenbos, Thermal quenching of lanthanide luminescence via charge transfer states in inorganic materials, J. Mater. Chem. C 11 (2023) 8129–8145, https://doi.org/10.1039/D2TC04439K.
[41] W.T. Carnall, G.L. Goodman, K. Rajnak, R.S. Rana, A systematic analysis of the spectra of the lanthanides doped into single crystal LaF_3, J. Chem. Phys. 90 (1989) 3443–3457, https://doi.org/10.1063/1.455853.
[42] G. Hovhannesyan, V. Boudon, M. Lepers, Transition intensities of trivalent lanthanide ions in solids: extending the Judd-Ofelt theory, J. Lumin. 241 (2022) 118456, https://doi.org/10.1016/j.jlumin.2021.118456.
[43] M.H. Liu, Y. Zhang, W.B. Sun, Z.D. Fu, D.L. Zhang, Study on an application manner of Judd-Ofelt theory to a phosphor material, Opt. Mater. 108 (2020) 109993, https://doi.org/10.1016/j.optmat.2020.109993.
[44] V. Vasyliev, E.G. Víllora, Y. Sugahara, K. Shimamura, Judd-Ofelt analysis and emission quantum efficiency of Tb-fluoride single crystals: liTbF$_4$ and $Tb_{0.81}Ca_{0.19}F_{2.81}$, J. Appl. Phys. 113 (2013), https://doi.org/10.1063/1.4807649.
[45] K. Jakhar, M. Dalal, M.K. Sharma, H. Om, Probing the crystal chemistry, photoluminescence and Judd–Ofelt investigation of Tb^{3+}-activated $Ba_2Y_5B_5O_{17}$ phosphors, J. Mater. Sci. Mater. Electron. 33 (2022) 26299–26312, https://doi.org/10.1007/s10854-022-09313-3.
[46] Z. Wang, Z. Yang, P. Li, Q. Guo, Y. Yang, Luminescence characteristics of $LiCaBO_3$: tb^{3+} phosphor for white LEDs, J. Rare Earths 28 (2010) 30–33, https://doi.org/10.1016/S1002-0721(09)60044-2.